THESIS FOR THE DEGREE OF LICENTIATE OF PHILOSOPHY

Elements of modeling nanoparticle growth: Surface thermodynamics and dispersive interactions

Joakim Löfgren

Department of Physics
CHALMERS UNIVERSITY OF TECHNOLOGY
Göteborg, Sweden 2017

Elements of modeling nanoparticle growth:
Surface thermodynamics and dispersive interactions
Joakim Löfgren

© Joakim Löfgren, 2017

Department of Physics
Chalmers University of Technology
se-412 96 Göteborg, Sweden
Telephone 0046317722902

Chalmers reproservice
Göteborg, Sweden 2017

Elements of modeling nanoparticle growth: Surface thermodynamics and dispersive interactions

Joakim Löfgren
Department of Physics
Chalmers University of Technology

Abstract

Metal nanoparticles have in recent decades been the subject of intense research owing to their wide range of size and shape-dependent properties, which makes them interesting candidates for a variety of applications. Gold nanorods represent a particularly intriguing type of particle due to their tunable plasmonic properties. To benefit from these features, access to a large supply of high-quality, monodisperse nanorods is required, but has yet to be realized. The most facile route to obtaining nanorods is through seeded-mediated growth, a family of wet-chemical synthesis protocols. While such protocols have the potential of delivering high quantities of rods with finely tuned properties, progress is being hampered by a lack of theoretical understanding regarding the growth mechanism. The aim of this thesis is to lay the foundation for a comprehensive picture of the gold nanorod growth process. In particular, the role of the CTAB surfactant layer covering the nanorod surfaces is investigated. The discussion is based on first-principles density functional theory calculations, molecular dynamics simulations carried out in our research group, and a critical review of ideas found in literature. A framework for explaining experimental observations and predicting the outcome of synthesis processes as a function of their parameters is presented based on the surface phase diagram of CTAB. A key feature of the phase diagram, in addition to the conventional bilayer structure that is often assumed, is the existence of cylindral and spherical micelles. These micelles expose the underlying gold surface to incoming gold ions that fuel the growth. The importance of dispersive interactions in understanding transitions between the different phases is emphasized. Furthermore, different models for the anistropic growth are reviewed within the newly established framework, and are complemented by a discussion of the impact of the seed particle structure.

Keywords: anisotropic nanoparticles, gold nanorods, growth mechanism, modeling, thermodynamics, dispersive interactions, van der Waals forces, density functional theory, molecular dynamics, surface phase diagram, CTAB

LIST OF APPENDED PAPERS

This thesis is partially based on work presented in the following papers:

I **Understanding the Phase Diagram of Self-Assembled Monolayers of Alkanethiolates on Gold**
Joakim Löfgren, Henrik Grönbeck, Kasper Moth-Poulsen, and Paul Erhart
The Journal of Physical Chemistry. C, 120, 12059 (2016)

II **libvdwxc: a library for exchange correlation functionals in the vdW-DF family**
Ask Hjorth Larsen, Mikael Kuisma, Joakim Löfgren, Yann Pouillon, Paul Erhart, and Per Hyldgaard
Modelling and Simulation in Materials Science and Engineering, 25, 065004 (2017)

PUBLICATIONS NOT INCLUDED IN THIS THESIS

The following publications are outside the scope of this thesis:

Electric field-controlled reversible order-disorder switching of a metal surface
Ludvig de Knoop, Mikael Juhani Kuisma, Joakim Löfgren, Kristof Lodewijks, Mattias Thuvander, Paul Erhart, Alexander Dmitriev and Eva Olsson
In manuscript

The author's contribution to the papers:

I The author carried out the calculations as well as the analysis and wrote the paper.

II The author contributed to the benchmarking calculations and testing of the software.

Contents

1 Introduction

Nanoscience is defined as the study and development of systems having one or more dimensions lying in the range of 1 to 100 nm. At this length scale quantum mechanical effects can lead to new or altered properties of a material that would not manifest on a macroscopic scale.

Historically, the use of nanoscale systems long predates any theory or systematic attempt at understanding the underlying phenomena, as evidenced, e.g., in the stained glass of church windows, resulting from the interaction of light with nanoparticles present in the glass [1]. Only with the advent of modern physics during the 20th century has theoretical understanding, manufacturing and precise manipulation of such systems become possible. Today, nanoscience constitutes an enormous research field with applications ranging from consumer grade products to next generation technologies in electronics [2], medicine [3] and renewable energy systems [4].

Metal nanoparticles (NPs) represent a prominent family of nanosystems, consisting of solid particles of various different shape with all dimensions being in the nanoscale range. The smaller the NP, the more its behavior can deviate from a bulk sample due to an increased surface-to-volume ratio, leading, e.g., to an increase in reactivity or quantum confinement effects that alter the optical properties. Metal NPs produced at industrial scales can already be found in many everyday products such as fabrics with anti-bacterial coating provided by silver nanoparticles [5] or sunscreen containing NiO and TiO_2 nanoparticles that scatter harmful ultraviolet radiation. Metal NPs are also used in the chemical industry as catalysts. The chemical reactions take place at the surface of the catalyst particle and by tuning the particle properties the selectivity and reactivity can be optimized. In addition to these uses, NPs hold great promise for future applications. In the field of renewable energy there is a growing interest in using hydrogen as a fuel as it has a high energy density by weight, is plentiful and environmentally clean. The realization of a so-called hydrogen economy faces, however, many

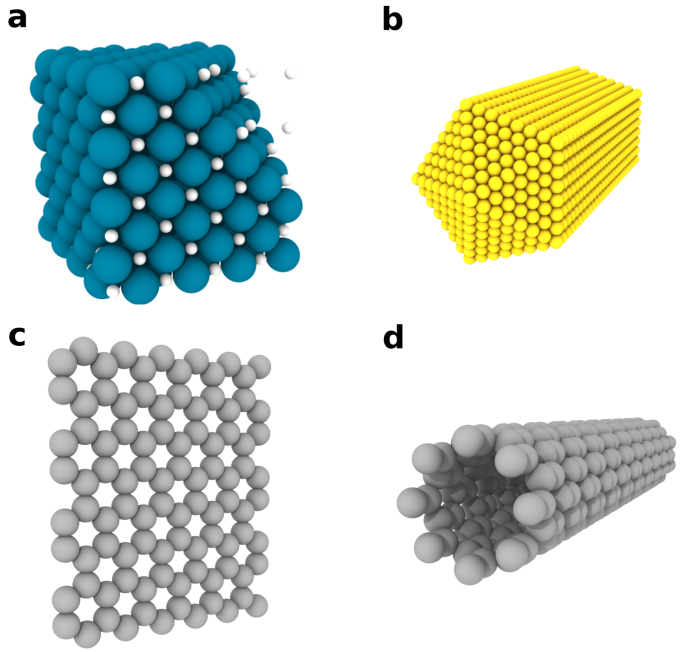

Figure 1.1: Various nanomaterials and their applications. **a)** Hydrogen storage in a Pd cube (one corner cut for visibility) enables the devlopment of hydrogen sensing devices. **b)** The tunable optical properties of Au nanorods can be used for cancer treatment. Carbon allotropes such as **c)** graphene and **d)** carbon nanotubes have excellent mechanical properties that can enhance the strength of materials.

obstacles, with one concern being safety since fuel leakage can lead to volatile mixtures of hydrogen and air. Here, sensors based on palladium NPs have been proposed as a possible solution, utililzing in different ways the fact that hydrogen can be stored in the palladium lattice (Fig. 1.1a) and form a hydride [6, 7].

The NP shape is typically critical for the application since it can have profound effects on the properties. This is especially true for gold nanorods (Fig. 1.1b) where the anisotropy is responsible for the splitting of the local surface plasmon resonance (LSPR) into one longitudinal and one transversal mode. The frequency of the longitudinal resonance mode is tunable through the aspect ratio of the rod, thus providing control over the optical response of the rod, since incident light at the resonant wavelength will be strongly adsorbed. This is the basis of photothermal cancer therapy where nanorods are targeted at a tumor and subsequently irradiated at the LSPR frequency. The adsorbed light is then given off as heat to the environment, resulting in the destruction

of the cancer cells.

Nanomaterials also come in many other forms, for instance, as allotropes of carbon where graphene [8] (Fig. 1.1c) has attracted significant interest from the scientific community in recent years due to its remarkable mechanical and transport properties. Closely related to graphene are carbon nanotubes [9] (Fig. 1.1d) that have, owing to their great tensile strength, stiffness and low weight, been used to make composite materials to enhance, e.g., sporting equipment [10] or vehicles.

1.1 Challenges for nanotechnology

Despite the potential of nanoparticle-based technologies, many of the applications are still in their infancy and there is no shortage of challenges that have to be addressed before they can be adopted for widespread use. One challenge concerns up-scaling; industrial production requires cost-effective manufacturing processes while historically nanoparticles have been created in specialized laboratories using time-consuming methods and expensive materials. In the recent decades, top-down methods have emerged as a scalable route to obtaining nanomaterials for use in, e.g., electronics. They are, however, less suited for nanoparticles since they often rely on surface modification via lithography. On the other hand, bottom-up, wet chemical synthesis offers a simple way of obtaining nanoparticles where properties of the products such as size, shape and composition are tunable through various synthesis parameters and components. A key issue here, however, is the lack of theoretical understanding concerning the synthesis processes themselves. Consequently improvements to protocols are mainly due to heuristics and ad hoc experimentation rather than the result of a rational design process, an approach that is ultimately limited.

From a societal perspective, there are also safety issues regarding nanotechnology as a whole, including toxicity, environmental pollution and the development of nanomaterial-based weaponry. For instance, the interactions of NPs with complex biological environments such as the inside of a human body are in general not well understood. The small size of the particles facilitates transport through the body and provides a large available surface for interactions with surrounding biomolecules. Indeed, studies have concluded that NPs entering the human body through the airways [11] or gastrointestinal tract [12] can be taken up in the blood circulation and be distributed to various organs via the liver and the spleen. The clearance rate of NPs from the body depends on the specific particle properties and may proceed via different mechanisms [13]. Long term retention of NPs leads to concerns regarding, e.g., cell damage as the result of excess generation of reactive oxygen species due to the presence of the particles [14]. There is thus a need for detailed experimental as well as theoretical studies with regards to the interactions in the interfacial region between NP surface and organic molecules.

1.2 Thesis outline

This thesis constitutes a contribution towards the larger effort of furthering the theoretical understanding of anisotropic nanoparticle growth. More conceretly, the main goal is a comprehensive, mechanistic understanding of the wet chemical synthesis of gold nanorods (AuNRs). This poses a formidable challenge, hence the scope of the thesis is limited to cover elements of the growth related to surface thermodynamics and dispersive interactions, with atomistic modeling as the primary investigative tool.

A background on colloidal nanoparticles including a brief historical perspective, fabrication methods, stability, and optical properties is provided in Chapter 2. In particular, wet-chemical synthesis of gold nanorods via seed-mediated growth is introduced and the properties of the resulting rods thus obtained are described. Surface thermodynamics is the topic of Chapter 3, which introduces a model for phase stability in adsorbate-adsorbent systems and the Wulff construction for determining equilibrium shapes of nanoparticles. Chapter 4 is devoted solely to understanding the growth of AuNRs. The problem is subdivided into several *aspects* in order to facilitate a systematic analysis, where the aspect of the surfactant layer structure is given a particularly extensive treatment. Theoretical basis for the computational methods employed can be found in Chapter 5, mainly restricted to density functional theory. Here, an important topic is that of dispersion-corrections, which play a prominent role in both of the appended papers (summarized in Chapter 6). Finally, Chapter 7 gives an overview and estimated timeline for future work, with general descriptions for many planned publications.

2

Colloidal nanoparticles

Elements combine and change into compounds. But that's all of life, right? It's the constant, it's the cycle. It's solution, dissolution. Just over and over and over. It is growth, then decay, then transformation.

Walter White

A colloid is a two-phase mixture with one discrete phase consisting of molecules or particles with sizes ranging from the nanometer to the micron scale, dispersed in a continuous phase. The particles are furthermore required to follow Brownian dynamics so that the mixture is stable against settling. Colloids can be divided into several subcategories. For example, emulsions are colloidal systems where one liquid is dispersed in another liquid, with everyday examples such as milk and egg yolk. This thesis, however, is concerned with suspensions of nanoparticles, i.e., solid particles dispersed in a liquid, known as a sol. Other examples of sols include blood, ink, and paint.

2.1 Historical highlights

The scientific study of colloidal nanoparticles began in the 1850s with Michael Faraday, who was interested in the optical properties of thin gold sheets [15]. As a by-product of this research he obtained a gold sol (Fig. 2.1) and began a systematic investigation of colloidal gold created from the reduction of a solution of gold chloride by phosphorus. He deduced, among other things, that the characteristic red tint of the sol was due to the interaction of light with suspended gold particles invisible to the naked eye [15]. Colloid science as a whole, however, did not start to pick up momentum until the end of the 19th century. In particular regarding nanoparticles there are several highlights

from this period. The first synthesis of colloidal silver from reduction of silver citrate by iron(II) citrate was carried out in 1889 by Lea [16]. Building on the work of Faraday, Zsigmondy invented the nucleus method in 1905 for the synthesis of gold sols [17]. Chloroauric acid ($HAuCl_4$) was reduced by white phosphorus creating a solution of nanoparticle seeds 1-3 nm in diameter. To obtain larger nanoparticles a growth solution was prepared in a vial and initially kept separate from the seeds. This growth solution contained more gold salt, which was reduced with formaldehyde. Addition of the seeds to this growth solution resulted in the formation of gold nanoparticles 8 to 9 nm in diameter. As will become clear below, this method of nanoparticle preparation has served as inspiration for the modern synthesis of anisotropic nanoparticles.

Significant advancements were also made on the theoretical side. The rapid motion undergone by suspended colloidal particles and their stability against gravity was explained in terms of Brownian motion by Einstein [18] and Smoluchowski [19]. The optical properties of metal sols were elucidated by Mie [20] and Gans [21], who derived shape-dependent expressions for the scattering and absorption of incident light by the particles from Maxwell's equations, providing an explanation for the observations made by Faraday some fifty years earlier.

Figure 2.1: A gold sol synthesized by Michael Faraday. Original, intact samples such as this one are on display in the Faraday museum of the Royal Institution, London. Faraday attributed the red coloring of the sample to the interaction of suspended gold particles with light decades before the theory of scattering by small particles was formulated. (Photo credit: Paul Wilkinson)

2.2 Fabrication methods

Fabrication of nanomaterials is often categorized as being either top-down or bottom-up. A top-down method starts from a bulk sample and then successively removes material until the desired shape or form is obtained as done in, for instance, optical or

electron lithography. Conversely, bottom-up fabrication is the assembly of a nanomaterial from smaller constituent pieces. Both categories of nanofabrication have their distinct advantages and limitations, but only bottom-up, wet-chemistry approaches will be dealt with here since they provide the most facile route to obtaining nanoparticles while top-down methods are more suitable for, e.g., surface patterning [22].

There are two principal approaches to bottom-up fabrication: gas-phase and wet-chemical (liquid-phase) synthesis. A gas-phase method starts from a precursor which is evaporated, forming an intermediate state containing monomers[1]. Nucleation in this intermediate state then leads to primary particles that form nanoparticles, e.g., by coalescing [23]. The resulting colloid of solid particles suspended in a gas is known as an *aerosol*. Liquid-phase synthesis processes follow a similar pattern. A precursor is created, for instance by dissolution of a solid, and an intermediate state of monomers is produced from chemical reactions. Nucleation in the monomer solution then leads to primary particles that subsequently form nanoparticles through e.g., diffusive growth [24]. Generally, gas-phase routes yield very pure product particles with minimal by-products, and scale better than their liquid-phase relatives. When it comes to the fabrication of anisotropic shapes, however, wet-chemical synthesis is the superior approach.

One example of a wet-chemical synthesis protocol has already been encountered, namely Zsigmondy's nuclear method described in the previous section. Another relevant example is the Turkevich method [25], which is one of the most commonly employed protocols for the synthesis of spherical gold nanoparticles[2]. A solution of chloroauric acid is heated to its boiling point and then a solution of sodium citrate ($Na_3C_6H_5O_7$) is added. The sodium citrate will act both to reduce the gold and as a capping agent for the subsequently formed nanoparticles, electrostatically stabilizing them against agglomeration by forming a negatively charged surface layer.

2.2.1 Seeded growth

Shape-controlled wet-chemical synthesis of metal nanoparticles is perhaps most easily achieved based on the concept of seeded, or seed-mediated, growth. Much like in Zsigmondy's nucleus method, the key characteristic of seeded growth is the preparation of a nanoparticle seed solution, which is later added to a separately prepared growth solution in order to achieve the desired product. The decoupling of the nucleation and growth stages allows for better control over size and shape of the final particles, at the cost of a more laborious synthesis process compared to one-pot protocols. Modern seeded growth began with the synthesis of gold nanorods in 2001 by Murphy and coworkers [26], who also demonstrated that it could be used to achieve greater size control when synthesizing spherical gold nanoparticles [27]. Following the same gen-

[1] In this text, a monomer refers to a unit of the precursor compound that supplies the growth.

[2] It can also be used to obtain silver nanoparticles.

eral principles, seed-mediated growth protocols have since been reported for a variety of other metals such as Ag, Pd, Pt and Cu [28, 29, 30].

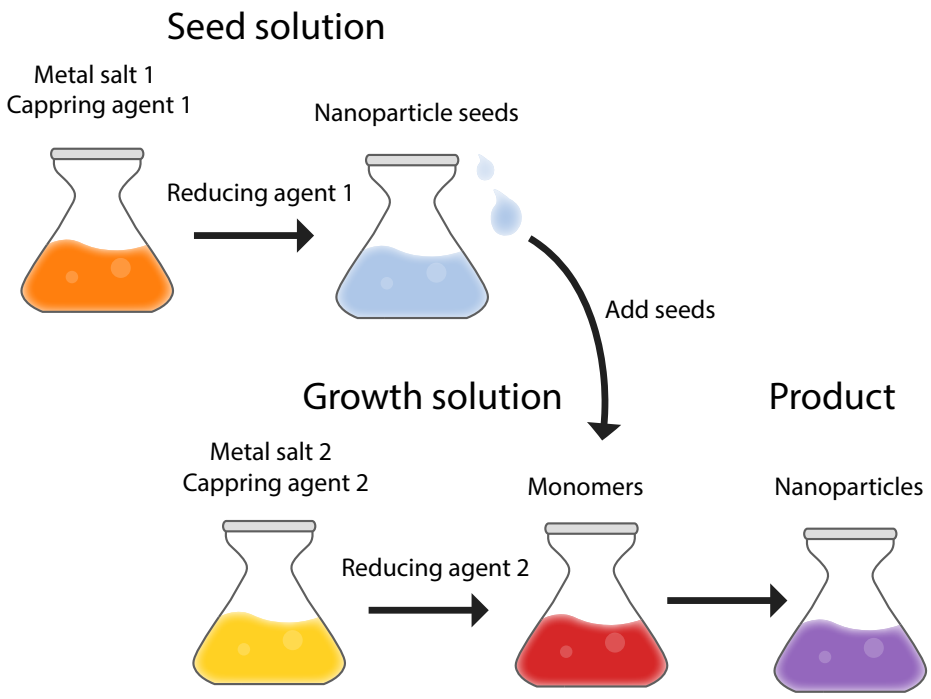

Figure 2.2: A general outline for seeded-mediated growth protocols. Decoupling the nucleation and growth stages by the separately synthesizing seeds and then adding them to a growth solution of monomers allows for more precise shape and size control. Depending on the desired outcome, metal salt and capping agents can vary between the two solutions. The growth solution reducing agent is constrained by the requirement that no additional nucleation can take place.

In a typical seeded growth protocol the seed solution will consist of a metal salt, a reducing agent and a capping (stabilizing) agent (Fig. 2.2) to prevent aggregation of the seeds and possibly alter the surface energetics to expose certain facets. The growth solution has the same basic ingredients but different compounds may be used depending on the goal of the synthesis. For instance, another type of metal salt may be used if bimetallic structures are targeted [31]. Furthermore, the rationale behind the seeded growth is that the growth solution reducing agent must be sufficiently weak to prevent the nucleation of additional seeds. This allows for metal ions to be reduced in a catalytic reaction near the surface of the seeds [26]. The resulting growth of the pre-existing seeds can then be guided towards anisotropic shapes by adding a second capping agent. In practice, the basic synthesis recipe described here is often augmented

with additives or co-surfactants in order to improve yield, monodispersity or to achieve different shapes. In terms of the growth stage, one can distinguish between one-step and multi-step protocols [32]. The latter are characterized by several iterated growth cycles, during which more growth solution is added to aliquots drawn from the current seed/growth solution mix.

It must be noted that deciphering the precise role played by the various ingredients is very difficult as they may vary on a method-to-method basis and synergistic effects can make the individual impact of a compound hard to disentangle from the whole. The descriptions provided above, while intuitive, are too simplistic to adequately account for the myriad permutations of seeded growth protocols.

2.3 Gold nanorods

Gold nanorods are the most extensively studied synthesis products of seed-mediated growth owing to their physicochemical properties, spurring research into a multitude of potential applications in, e.g., drug delivery, cancer therapy and sensing. Furthermore, they also pose a very interesting problem from a theoretical perspective with many questions that remain unanswered regarding, e.g., the origin of the symmetry breaking event that occurs in the evolution from spherical seeds to nanorods. As the first seeded growth method to gain widespread popularity it is also particularly appropriate as a concrete illustration of the generalized description presented in Sect. 2.2.1.

2.3.1 Nomenclature

Before discussing the details of the gold nanorod synthesis protocols, it is convenient to introduce some nomenclature regarding the geometry and crystalline structure of a nanorod. The terms are adopted with the purpose of eliminating ambiguity in the discussion of the structure of the synthesized rods and are chosen in the spirit of [33]. Accordingly, the *orientation* or *growth direction* of a rod refers to the elongated direction and the facets perpendicular[3] to this direction are called *prism* facets. The end of the rod is referred to as the *termination* and may be either *basal*, *pyramidal* or *truncated pyramidal*. A basal termination consists of a single *terminal* facet parallel to the orientation while a pyramidal termination consists of *pyramidal* facets angled intermediately between a prism and terminal facet. The truncated pyramidal termination may contain a mix of terminal and pyramidal facets.

[3]The direction of a facet is taken to mean that of its surface normal.

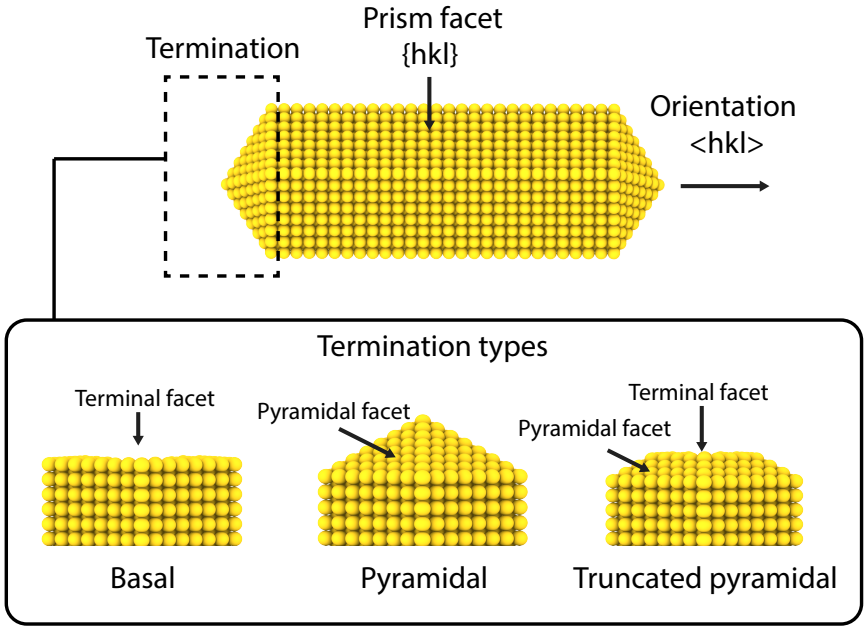

Figure 2.3: Nomenclature used in describing nanorod geometry. The rod has an overall orientation corresponding to the elongated growth direction. The two ends, or terminations, are categorized as basal, pyramidal and truncated pyramidal. The facets perpendicular to the rod orientation are called prism facets while the terminations can expose terminal and pyramidal facets.

2.3.2 Synthesis

Turning to the actual nanorod synthesis procedure, it should be noted that since its advent many variations of the original protocol have spawned that try to improve, e.g., yield or control over the aspect ratio (AR). The latter is especially important since it allows for tuning the plasmonic response (see section on optical properties of nanoparticles). Rather than providing an exhaustive list of all possibilities, focus will be on the original three-step protocol by Murphy [26] and the nowadays more commonly employed silver-assisted one-step protocol [34].

Three-step protocol (P-1). This protocol follows the general seeded growth procedure outlined in Fig. 2.2. The seeds are prepared by reducing $HAuCl_4$with ice-cold sodium borohydride[4] ($NaBH_4$) and adding sodium citrate (citrate) to stabilize the seeds against aggregation. In the growth solution the reduction of $HAuCl_4$is instead accomplished with ascorbic acid (AA) in the presence of cetyltrimethylamoniumbromide (CTAB) surfactant (Fig. 2.4). It should be noted here that a concentration of around

0.1 M CTAB is required in order to obtain nanorods, which is 100 times more than the first critical micelle concentration (CMC), 1.0 mM, of CTAB [35]. The rods are grown iteratively in three steps and the final solution must be left for several hours to attain maximal growth. The rods thus synthesized are oriented along [110] and have a penta-twinned structure. In an idealized model the prism facets are all {100} (Fig. 2.5a), but in practice the facets are often found to be mix between {100} and (110) [36]. The termination is pyramidal and consists of {111} facets (Fig. 2.3). The AR ranges between 10 to 25 and the length of a fully grown rod can be in the lower micron range [37] (Fig. 2.6).

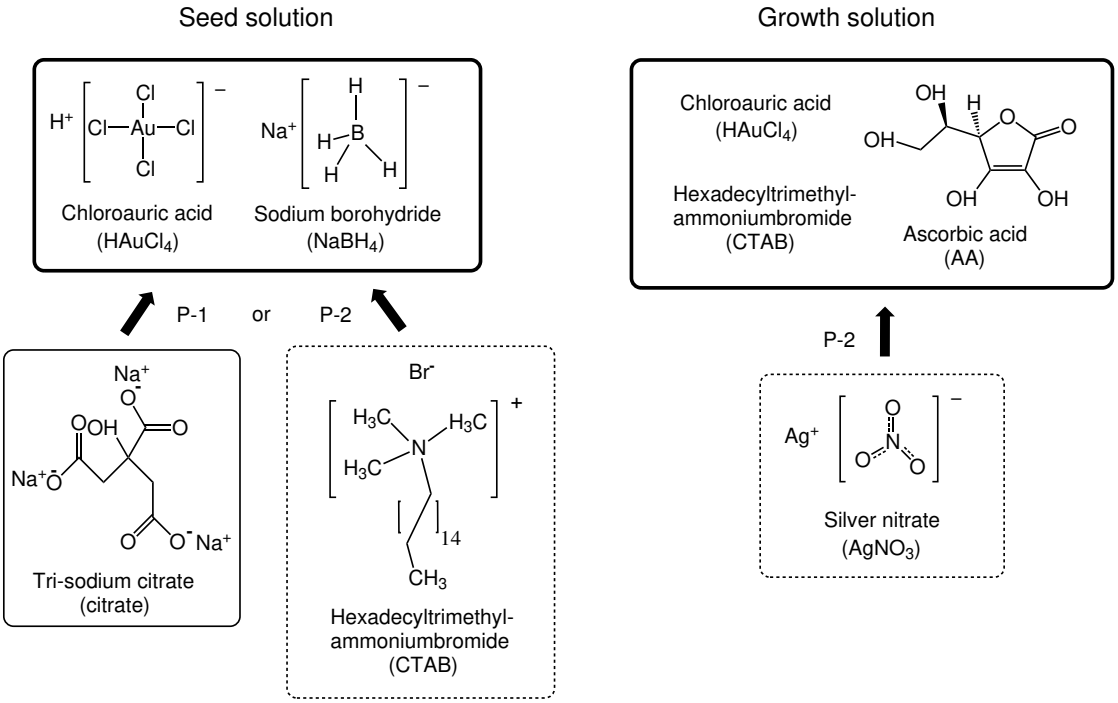

Figure 2.4: Chemical structural formulas and names of the compounds used in the seeded growth of gold nanorods via either the **P-1** or the **P-2** protocol. In a **P-2** synthesis, the CTAB replaces citrate as the stabilizing agent in the seed solution and a small amount of silver nitrate is added to the growth solution.

A significant shortcoming with the **P-1** protocol is that the initial yield of nanorods by shape is only about 5% before purification. It turns out there is a much simpler way of obtaining nanorods in high yield by a few straightforward modifications to **P-1**.

Silver-assisted protocol (P-2). In this synthesis protocol, CTAB replaces sodium citrate as the capping agent in the seed solution and silver nitrate ($AgNO_3$) is added in small amounts to the growth solution (Fig. 2.4). Nanorods are subsequently grown in a single step, yielding rods with ARs that can be precisely varied between 2 to 5 by changing the silver concentration. The overall dimensions of these rods are significantly smaller compared to the **P-1** rods, with typical rod lengths under 100 nm [37]. Furthermore, the nanorods have an octagonal cross-section and are single-crystalline rather than penta-twinned. While no broad consensus has been achieved with regards to the faceting, several studies suggest the presence of high-index prism facets such as {520} [38], or possibly a mix between such facets and {100}/{110} [39]. The termination is truncated pyramidal and exposes mix of alternating {111} and {110} facets.

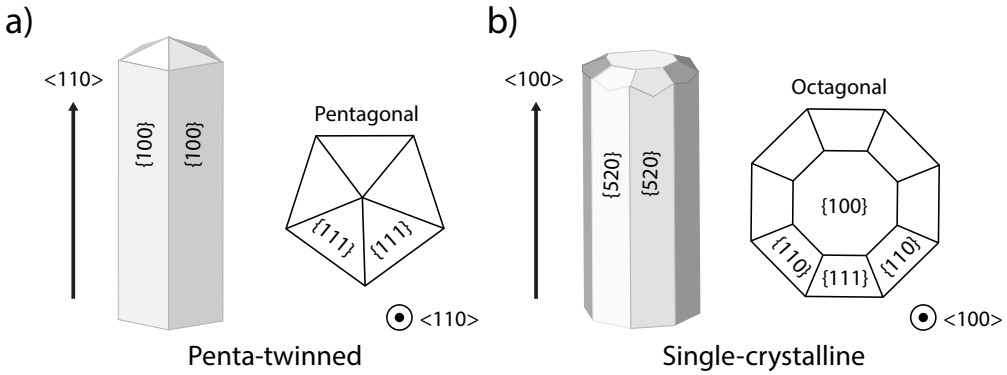

Figure 2.5: Proposed models, including cross-sections views, for the faceting of gold nanorods. a) The three-step protocol yields penta-twinned nanorods with a pyramidal termination. b) For the silver-assisted protocol, a single-crystalline structure with an octagonal cross-section is obtained. Different models have been proposed for the faceting, shown here is one based on high-index {520} prism facets.

Many attempts at further improvement of the silver-assisted growth protocol have been made by introducing various additives such as organic molecules and acids. A notable example is the introduction of a co-surfactant in the form of sodium oleate (NaOl), which has been observed to produce nanorods with a 99.5% yield and tunable AR [40]. Interestingly, the amount of CTAB required for this synthesis is around three times lower than what is commonly used for nanorod synthesis.

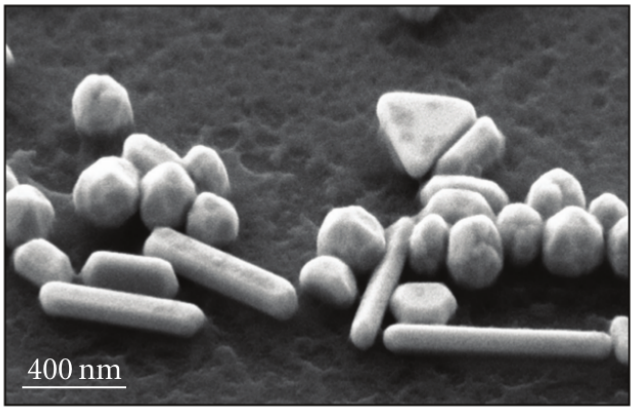

Figure 2.6: The products of a **P-1** synthesis imaged at an angle using a scanning electron microscope [41]. Note that in addition to high-aspect ratio gold nanorods, a variety of other shapes is obtained as well.

2.4 Optical properties

Much of the scientific interest in nanoparticles stems from the fact that they can exhibit localized surface plasmon resonances (LSPR), giving rise to shape-dependent absorption and scattering. Given sufficient understanding of the correlation between particle shape and the synthesis parameters, the optical properties of the nanoparticles can thus be controlled. As previously mentioned, the mathematical theory of interaction between light and colloidal particles started with Mie in 1908 [20], who derived analytical expressions describing the absorption and scattering of small spherical particle using classical electromagnetic theory. Only a brief summary of some especially pertinent results will be given here, for a more complete treatment the reader is referred to, e.g., [42].

The LSPR can be understood as a collective oscillation of electrons close to the surface of a nanoparticle that is excited by an external electric field (Fig. 2.7). The electrons behave similarly to a harmonic oscillator under the influence of a harmonic external force and there exists a certain resonance frequency, for which the amplitude attains a maximum[5]. Consequently, light propagating through a nanoparticle sol will be absorbed and scattered by the particles. After traversing a length L, the intensity of the light will have decayed according to the Beer-Lambert law

$$I(L) = I_0 \exp(-\rho_N C_{\text{ext}} L), \tag{2.1}$$

[5]A more apt analogy would be that of a damped driven harmonic oscillator in order to take the plasmon decay into account.

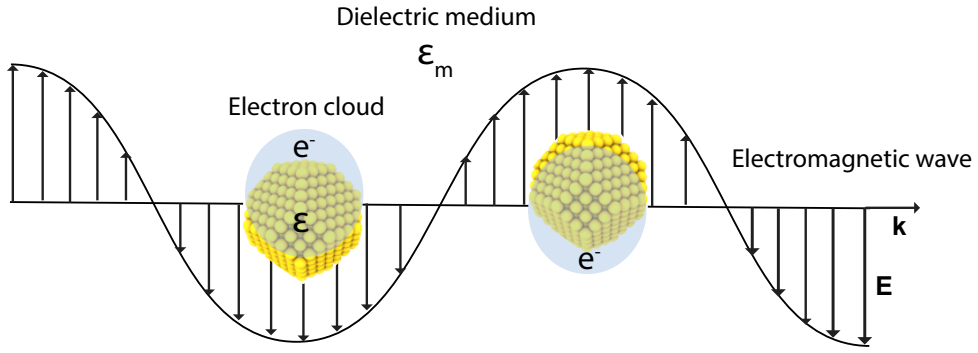

Figure 2.7: A schematic illustration of a localized surface plasmon resonance in a nanoparticle. An external electromagnetic wave with the right frequency can a excite a collective oscillation of the electron cloud near the surface of the particle.

where I_0 is the initial intensity, ρ_N the number density, and C_{ext} the so-called extinction cross section, which is defined as the sum of the absorption and scattering cross sections $C_{\text{ext}} = C_{\text{ads}} + C_{\text{sca}}$. In the case of an electromagnetic wave incident on a spherical particle of radius a and surrounded by a dielectric medium, Maxwell's equations may be solved by series expansions and exact expression for the cross sections can be found in terms of infinite series. These are very laborious to compute, but in the Rayleigh-limit where the scattering particle is assumed to be smaller than the wavelength λ of the incident light simple formulas can be found. Assuming the particles are immersed in a medium with dielectric constant ϵ_m and the external field has wavenumber $k = 2\pi\lambda$ they read

$$C_{\text{abs}} = 4\pi k a^3 \text{Im}\left\{\frac{\epsilon - \epsilon_m}{\epsilon + 2\epsilon_m}\right\} \tag{2.2}$$

and

$$C_{\text{sca}} = \frac{8\pi}{3} k^3 a^6 \left(\frac{\epsilon - \epsilon_m}{\epsilon + 2\epsilon_m}\right)^2. \tag{2.3}$$

Maximum extinction is achieved if the denominator $|\epsilon + 2\epsilon_m|$ in Eqs. (2.2) and (2.3) is minimized. Assuming $\text{Im}\{\epsilon(\omega)\}$ varies slowly around the minimum, the condition becomes

$$\text{Re}\{\epsilon(\omega)\} = -2\epsilon_m. \tag{2.4}$$

Frequencies for which this relation is satisfied are termed LSPR frequencies.

Further insight into the behavior of these oscillatory modes can be gained by assuming a free electron gas model for the conduction electrons in the metal nanoparticle. The dielectric function $\epsilon(\omega)$ is then given by

$$\epsilon(\omega) = 1 - \frac{\omega_p^2}{\omega^2 + i\gamma\omega}, \tag{2.5}$$

and substitution of this expression into the plasmon resonance condition Eq. (2.4) shows that maximum extinction will occur for frequencies that satisfy

$$\omega_{\max} = \omega_p \sqrt{2\epsilon_m + 1}. \tag{2.6}$$

From this equation it is clear that the location of the plasmon resonance depends on the dielectric environment of the particle and it is this effect that forms the theoretical basis for the use of plasmonic nanoparticles in sensing applications.

Mie's work was later extended by Gans, who considered the more general case of ellipsoidal particles [21]. This result is of particular interest since an ellipsoid with axes $a > b = c$, i.e. a prolate spheroid, can be used to approximate a nanorod for which no analytical formulas are otherwise available. Note that the scattering will now depend on the orientation of the rod with respect to the incident electromagnetic wave. To describe colloidal nanorods it is thus appropriate to assume an ensemble of randomly oriented prolate spheroids and then calculate the average cross section yielding

$$\langle C_{\text{ext}} \rangle = \frac{2\pi V \epsilon_m^{3/2}}{3\lambda} \sum_{i \in \{a,b,c\}} \frac{(\epsilon/P_i)^2}{\left(\text{Re}\{\epsilon\} + ((1-P_i)/P_i)\epsilon_m\right)^2 + \text{Im}\{\epsilon\}^2}. \tag{2.7}$$

Here, V is the volume of a spheroid and P_i are shape-dependent factors given in terms of the eccentricity $e = \sqrt{(a^2 - b^2)/a^2}$ with

$$P_a = \frac{1-e^2}{e^2}\left(\frac{1}{2e}\log\left(\frac{1+e}{1-e}\right) - 1\right) \tag{2.8}$$

and

$$P_b = P_c = \frac{1 - P_a}{2}. \tag{2.9}$$

Equation (2.7) yields extinction spectra that display two peaks. The single plasmon resonance found for a spherical particle is thus split into two resonances, corresponding to one transverse and one longitudinal mode, respectively. It is interesting to study the spectral shift of the resonances as a function of the aspect ratio AR $= a/b$ of the spheroids (Fig. 2.8). While the transverse mode is largely unaffected except for a minuscule blueshift, the longitudinal mode experiences a large redshift as the AR increases. This behavior is indeed experimentally observed for real gold nanorods. As described in the introduction, the tunability of the longitudinal resonance peak is one of the main driving forces behind the extensive research surrounding gold nanorods as it holds the

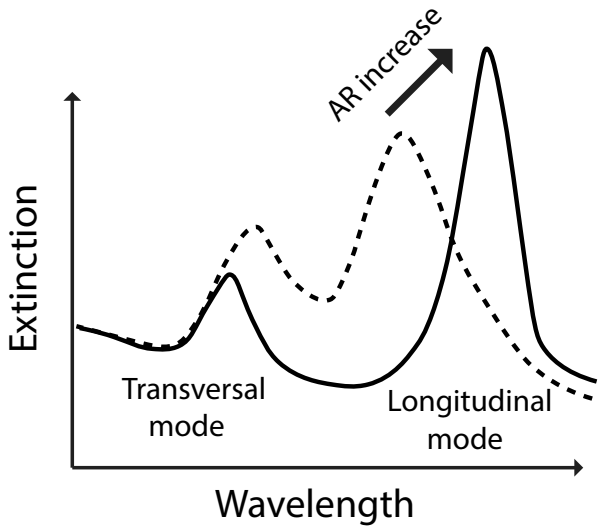

Figure 2.8: A schematic illustration of the extinction spectrum of a spheroidal nanoparticle for two different aspect ratios. The anisotropy causes the plasmonic resonance of the particle to split into a transversal and a longitudinal mode. As the aspect ratio increase the longitudinal resonance peak is redshifted, while only a small blueshift is observed for the transversal peak.

key to many applications. The plasmonic behavior of the rods thus illustrates the importance of a thorough understanding of how the synthesis protocol affect the product particles in terms of morphology, size and composition in the case of alloy NPs.

2.5 Colloidal stability

In the context of colloidal science, the word *stability* is not used in the thermodynamic sense of a system state that corresponds to the minimum of a thermodynamic potential since this would necessarily imply a phase separation. Rather, colloidal stability typically refers to a thermodynamically metastable state in which the system has become kinetically trapped. In this state the discrete phase remains dispersed in the continuous phase without settling or precipitating, a condition which requires the particles to obey Brownian dynamics. In practice, most colloids do settle and reach thermodynamic equilibrium over time. The rate of this process can vary dramatically, milk settles over a span of a few weeks while Faraday's gold sols (Fig. 2.1) have remained intact for more than 150 years.

Restricting the discussion to the case where the discrete phase consists of particles

with mass m, a limiting size for the Brownian regime can be obtained [43]. Consider the distribution of particles at height h in a continuous medium of density ρ_m. In equilibrium this distribution follows Boltzmann statistics with weights determined by the gravitational potential energy

$$P(h) \propto \exp\left(-\frac{mgh}{k_B T}\right). \tag{2.10}$$

Accordingly, the distribution has a mean value $\langle h \rangle = k_B T/mg$. Assuming the particles are spherical with radius a and density ρ, they are suspended if $\langle h \rangle > 2a$, which solving for a and adjusting the density to include buoyancy yields

$$a < \left(\frac{3k_B T}{8\pi g(\rho - \rho_m)}\right)^{1/4}. \tag{2.11}$$

For, e.g., gold particles in water under ambient conditions this requirement yields an upper limit of $a \lesssim 0.5\,\mu$m. Note, however, that even if a suspension initially contains only particles of dimensions consistent with Eq. (2.10), the criterion may still be violated. This occurs if the attractive inter-particle forces in the systems are stronger than their repulsive counterparts, in which case neighboring particle adhere to each other and *coalesce* or form *aggregates* that settle when they reach the limiting size.

2.5.1 van der Waals interactions

The driving force behind adhesion of colloidal particles comes from dispersive interactions, which are long-ranged, attractive, and present in all atomic systems. These interactions can, at least partially, be understood in terms of a semi-classical picture: quantum mechanical charge fluctuations create an instantaneous dipole in an atom A, which subsequently induces an aligned, instantaneous dipole in a neighboring atom B. The result is an interaction between the two induced dipoles AB that is always favorable and decays as $1/r^6$. The true origin of dispersive interactions is, however, purely quantum mechanical and the reader is referred to Appendix A for a more detailed discussion. Dispersive interactions are often referred to as *van der Waals* (vdW) interactions, although some authors use this term to also include dipole-induced dipole (Debye) and dipole-dipole (Keesom) interactions. In contrast to the dispersive interactions, the Debye and Keesom interactions can be adequately described by classical physics [44]. In this work the terms van der Waals and dispersive interactions are used synonymously.

An expression for the vdW interaction energy between two spherical particles can be derived by assuming that the microscopic contribution from an atomic pair follows the asymptotic $1/R^6$ form. The total vdW energy is then additive and given by

$$U_{\mathrm{vdW}} = -\sum_{I\mathcal{J}} \frac{C_6^{I\mathcal{J}}}{R_{I\mathcal{J}}^6}, \tag{2.12}$$

where $C_6^{I\mathcal{J}}$ are coefficients that determine the strength of the interaction between two atoms $I, \mathcal{J}$ at a fixed separation $R_{I\mathcal{J}}$. It is assumed for simplicity that the particles are of identical, homogeneous composition and volume $V_1 = V_2$. Note that the summation in Eq. (2.12) runs over all atoms $I \in V_1$ and $\mathcal{J} \in V_2$. Now denote by AB the basic building block of the particle, it can be e.g., a single atom or a compound. Furthermore, let $\rho \equiv \rho_{AB}$ be the number density of such building blocks and $C_6 \equiv C_6^{AB,AB} = C_{AA} + 2C_{AB} + C_{BB}$ the vdW coefficient. In the continuum limit Eq. (2.12) can then be recast as a double integral over the two spherical volumes,

$$U_{\mathrm{vdW}} = -\int_{V_1} dR_1 \int_{V_2} dR_2 \rho^2 \frac{C_6}{\left|R_1 - R_2\right|^6}. \tag{2.13}$$

This integral was first carried out analytically by Hamaker [45], who obtained

$$U_{\mathrm{vdW}} = -\frac{A_h}{6}\left(\frac{2a^2}{R^2 - 4a^2} + \frac{2a^2}{R^2} + \log\left(\frac{R^2 - 4a^2}{R^2}\right)\right), \tag{2.14}$$

for spheres of radii a and center-to-center distance R. The constant $A_h = -\pi^2\rho^2 C_6$ appearing in Eq. (2.14) is accordingly referred to as the *Hamaker constant*.

2.5.2 Electrostatic interactions and DLVO theory

In order to stabilize the colloidal particles against aggregation or coalescence the net inter-particle forces must be repulsive. One way to stabilize the particles is via so-called electrostatic stabilization[6], where the surface charge of the particles is tuned so that they repel each other. There are many pathways through which a particle surface can acquire a net charge. These include, for instance, adsorption of a charged species, dissociation of a surface species into charged fragments as well as the build-up of a positive or negative excess of electrons at the surface. Once the surface has become charged, oppositely charged species are attracted towards it forming an electric *double layer*.

Limiting the discussion to colloidal particles in ionic solutions, which is the setting relevant for wet-chemical synthesis processes, an illustrative derivation of the electrostatic interaction between two charged spherical particles is provided below. Detailed

[6]Another option is *steric stabililzation*, where polymers are grafted onto the particle surface. As two particles approach each other, an overlap region is created in which the confinement of the polymers leads to a loss of configurational entropy that manifests as a repulsive force.

accounts can be found in elementary textooks on electrolyte solutions [46]. The double layer charge distribution gives rise to an electric surface potential ϕ that can be obtained from the Poisson equation

$$\Delta\phi(\boldsymbol{r}) = -\rho(\boldsymbol{r}). \tag{2.15}$$

In equilibrium, the concentrations of each ionic species j with bulk concentration n_j^0 and charge q_j follow Boltzmann statistics and thus the total charge distribution on the right-hand side of Eq. (2.15) is given by

$$\rho(\boldsymbol{r}) = \frac{1}{\epsilon}\sum_j q_j n_j^0 e^{-q_j\phi(\boldsymbol{r}/(k_BT))}, \tag{2.16}$$

where $\epsilon = \epsilon_0\epsilon_r$ and ϵ_r is the dielectric constant of the medium. When combined, Eqs. (2.15) and (2.16) form the *Poisson-Boltzmann equation*. Note that the electric potential also appears in the Boltzmann factors in Eq. (2.16), making the Poisson-Boltzmann equation non-linear and thus very hard (or impossible) to solve. A common approximation is the *Debye-Hückel linearization*, obtained by Taylor expanding the Boltzmann factors to second order. If a symmetric electrolyte is assumed, the first order terms in this expansion cancel due to the charge neutrality condition and the resulting linearized Poisson-Boltzmann equation can be written compactly as

$$\Delta\phi(\boldsymbol{r}) = \kappa^2\phi(\boldsymbol{r}), \tag{2.17}$$

where the *Debye screening length*

$$\kappa^{-1} = \sqrt{\frac{\epsilon k_B T}{\sum_j n_j^0 q_j^2}} \tag{2.18}$$

has been introduced. Furthermore, if a spherically-symmetric charge distribution is assumed, Eq. (2.17) can be solved analytically. For instance, in the region outside of a spherical particle of radius a and total charge Q, the solution is given by a screened Coulomb (Yukawa) potential

$$\phi(r) = \frac{Q}{4\pi\epsilon}\frac{\exp(\kappa a)}{1+\kappa a}\frac{\exp(-\kappa r)}{r}. \tag{2.19}$$

An expression for the electrostatic interaction energy U_{elec} between two spherical particles can now be derived under the *superposition approximation*, which assumes that the particles are sufficiently separated so that the overlap between their double layers is zero. The interaction energy is then given by integration of the surface potential outside the first particle (Eq. (2.19)) over the surface of the second particle. Again denoting the center-to-center distance between the particles by R, the result is

$$U_{\text{elec}}(R) = \frac{Q^2}{4\pi\epsilon}\left(\frac{\exp(\kappa a)}{1+\kappa a}\right)^2 \frac{\exp(-\kappa R)}{R}. \tag{2.20}$$

The total interaction potential for the two particles is then the sum of Eqs. (2.20) and Eqs. (2.14)

$$U_{\text{tot}}(R) = U_{\text{vdW}}(R) + U_{\text{elec}}(R). \tag{2.21}$$

The force exerted by the particles on one another is simply the derivative of this expression and if it is repulsive the colloid is stable. Particle pair potentials of the form Eq. (2.21) is the subject of *DLVO theory*, a simple yet powerful framework for understanding colloidal interactions and stability.

2.6 Classical nucleation theory

The self-assembly of a nanoparticle in a solution has historically been described within the framework of classical nucleation theory (CNT) [47]. The word *nucleation* refers to the formation of localized embryos of a new phase in a supersaturated environment, which typically exhibits the characteristics of first order phase transitions. The nucleation process is termed *homogeneous* if it occurs uniformly throughout the environment and *heterogeneous* if it occurs in the vicinity of defects, interfaces or impurities. CNT considers the competition between the bulk free energy gain and interface free energy cost of an embryo. Limiting the discussion to a spherical particle of radius a, the total free energy barrier towards homogeneous nucleation can be written

$$\Delta G = \frac{4}{3}\pi a^3 g_{\text{bulk}} + 4\pi a^2 \gamma, \tag{2.22}$$

where g_{bulk} is the bulk free energy per unit volume and γ is the surface tension. The total free energy can be minimized to obtain critical radius and energy barrier

$$a^* = -\frac{2\gamma}{g_{\text{bulk}}}, \quad \Delta G^* = \frac{16\pi\gamma^3}{3g_{\text{bulk}}} \tag{2.23}$$

that define the lower size limit and free energy required to form a nucleus. The formation can occur spontaneously through thermal size fluctuations if ΔG^* is on the order of $k_B T$.

CNT thus provides a thermodynamic rationale for the first step of particle formation and is usually coupled with a mechanism for the subsequent growth of the nascent particles. A good example is the LaMer growth model [48]. It posits that nucleation of new particles proceeds quickly to the point where the concentration falls below supersaturation in a step called burst nucleation, after which growth of the existing particles proceeds through diffusion and attachment of monomers. Another possibility is Ostwald

ripening [49]: small particles that are unstable due to their high surface energy dissolve and provide growth material for larger particles. Frequently when nanoparticle growth is concerned, the term CNT takes on a broader meaning to include any model that invokes a nucleation process coupled with one of the aforementioned growth mechanisms.

3

Surface thermodynamics

God made the bulk; surfaces were invented by the Devil.

Wolfgang Pauli

3.1 Thermodynamic stability of adsorbate systems

A basic consideration for any surface system is the thermodynamic phase stability as a function of the chemical environment. The purpose of this section is to show that computational methods can be helpful in this endeavor by formulating a thermodynamic model of adsorption that takes as input total energies obtained from atomistic calculations and is able to predict under which conditions certain phases are thermodynamically stable [50, 51]. Adsorption is often categorized as either *chemisorption*, where a chemical bond is formed between adsorbate and surface, or *physisorption*, where the adsorbate is weakly bonded to the surface through van der Waals interactions. For the development of the aforementioned model, however, this distinction is not important.

Consider the interfacial region between an elemental crystal[1] M and a source of potential adsorbate molecules or atoms X. The surface $M\{hkl\}$ is assumed to be flat, single crystalline and initially without defects. The nature of the source, including phase, composition and properties such as dilution, is left unspecified for the moment. A non-dissociative the adsorption event (Fig. 3.1) can be represented as a reaction[2]

[1] The restriction to monatomic crystals is not strictly necessary but simplifies the discussion.

[2] In the case of dissociative adsorption when the source consists of molecules XY the dissociation must be included in the adsorption process. For example, if $X = Y$ the reaction becomes $M_{\text{surf}} + \frac{1}{2}X_2 \longrightarrow M_{\text{surf}} : X$.

$$M_{\text{surf}} + X \longrightarrow M_{\text{surf}} : X. \tag{3.1}$$

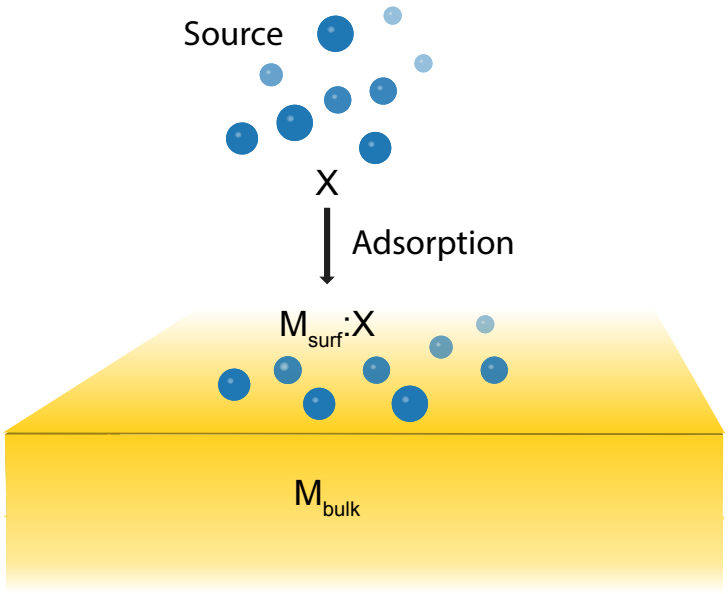

Figure 3.1: Non-dissociative adsorption on the surface of a material M in contact with a source of molecules X. This can be regarded as a reaction bringing the isolated surface and molecules together in an adsorbed state. The free energy of the reaction determines if it is endothermic or exothermic.

It is useful to generalize this reaction to allow for the possibility of a surface reconstruction. The number of M atoms in the interfacial region then undergoes a change $N_M \to N_M + \Delta N_M$ upon adsorption of N_X molecules. This net change can be expressed as $\Delta N_M = N_a - N_v$, where N_a is the number of adatoms and N_v is the number of vacancies. The stoichiometric reaction is then written as

$$N_M M_{\text{surf}} + N_X X \xrightarrow{A\Delta\gamma_{\text{ads}}} (N_M + \Delta N_M) M_{\text{surf}} : N_X X - \Delta N_M M_{\text{bulk}}, \tag{3.2}$$

where a change in free energy per area unit $\Delta\gamma_{\text{ads}}$ has been introduced that when multiplied by the area gives the total change in Gibbs free energy $\Delta G = A\Delta\gamma_{\text{ads}}$ associated with the reaction. The change in surface free energy is obtained by taking the free energy difference of the right and left-hand side of Eq. (3.2) and dividing by the area, leading to

$$\Delta\gamma_{\text{ads}} = \frac{1}{A}\left(G_{\text{surf}:X} - G_{\text{surf}} - \Delta N_M \mu_M^{\text{bulk}} - N_X \mu_X\right). \tag{3.3}$$

The terms in the right-hand side of Eq. (3.3) represent, going from left to right, the free energy of the surface with adsorbates, the free energy of the clean surface, the net change in M atoms ΔN_M times the chemical potential of the bulk μ_M^{bulk}, and the number of adsorbates N_X times the chemical potential of the molecules μ_X. Here, the bulk and the source are regarded as reservoirs: chemical potentials measure their propensity to exchange matter with the interfacial region.

The next goal is to write the chemical potential of the source in a convenient form, starting with the decomposition

$$\mu_X = \underbrace{E_X + \mu_X^{\text{vib}}}_{\equiv \mu_X^{\text{mol}}} + \Delta\mu_X. \tag{3.4}$$

In this form, contributions that are intrinsic to the X molecule, i.e., the internal energy E_X and the total vibrational contribution[3] μ_X^{vib} are grouped into μ_X^{mol}. The remaining terms in the total chemical potential depend on the state of the source and are correspondingly grouped into $\Delta\mu_X$. Another expression for the total chemical potential more convenient for comparison with experimental measurements comes from the definition of the activity a_X of species X,

$$\mu_X = \mu_X^\circ + k_B T \log\left(a_X\right). \tag{3.5}$$

Here, μ_X° is the chemical potential of the source in a reference state, the definition of which again depends on the nature of the source. By combining Eqs. (3.4) and (3.5) it follows that

$$\mu_X = \mu_X^{\text{mol}} + \underbrace{(\mu_X^\circ - \mu_X^{\text{mol}}) + k_B T \log\left(a_X\right)}_{=\Delta\mu_X}. \tag{3.6}$$

The purpose of writing the chemical potential in this way will become clear presently. Substitution of μ_X in Eq. (3.3) with the expression in Eq. (3.6) now yields

$$A\Delta\gamma_{\text{ads}} = \underbrace{G_{\text{surf}:X} - G_{\text{surf}} - \Delta N_M \mu_M^{\text{bulk}} - N_X \mu_X^{\text{mol}}}_{\equiv \Delta G_{\text{ads}}} - N_X \Delta\mu_X. \tag{3.7}$$

As indicated in the above equation, the first four terms on the right hand side can be collected into what will be referred to as the Gibbs free energy of adsorption ΔG_{ads}, in terms of which

$$\Delta\gamma_{\text{ads}} = \frac{1}{A}\left(\Delta G_{\text{ads}} - \Delta\mu_X\right). \tag{3.8}$$

[3] This includes the zero-point energy E_X^{ZPE} of the molecule.

From Eq. (3.3) it is clear that $\Delta\gamma_{\text{ads}} < 0$ when the formation of the adsorbate phase is exothermic with respect to the clean surface and that the most stable adsorbate phase is the one that minimizes $\Delta\gamma_{\text{ads}}$. More generally, the structure of the underlying surface $M\{hkl\}$ can also be allowed to vary if the total surface free energy of adsorption

$$\gamma_{\text{tot}}^{\{hkl\}} = \gamma_{\text{clean}}^{\{hkl\}} + \Delta\gamma_{\text{ads}}^{\{hkl\}} \tag{3.9}$$

is minimized instead.

Equations (3.8) and (3.9) provide the starting point for analyzing phase stability with the aid of computational methods that can be used to calculate the total (internal) energy contributions to the free energies in Eq. (3.7). Entropic contributions can be very hard to calculate, but it turns out that this is not always necessary. For instance, the difference in vibrational entropy of a molecule on the surface compared to that of a free molecule is often small. Under such conditions, a reasonable approximation is given by

$$\Delta G_{\text{ads}} \approx \Delta E_{\text{ads}}. \tag{3.10}$$

The Gibbs free energy of adsorption is thus replaced by the energy of adsorption, which can be written explicitly as

$$\Delta E_{\text{ads}} = E_{\text{surf}:X} - E_{\text{surf}} - \Delta N_M E_M^{\text{bulk}} - N_X E_X. \tag{3.11}$$

Instead of ΔE_{ads}, it is often more convenient to look at the average adsorption energy per molecule

$$\mathscr{E}_{\text{ads}} = \frac{\Delta E_{\text{ads}}}{N_X}, \tag{3.12}$$

and the corresponding expression for the change in surface free energy of adsorption becomes

$$\Delta\gamma_{\text{ads}} \approx \frac{N_X}{A}\left(\mathscr{E}_{\text{ads}} - \Delta\mu_X\right). \tag{3.13}$$

The expression above is a linear function of the relative chemical potential with a slope that is proportional to the coverage

$$\Theta = N_X \frac{A_{\text{prim}}}{A}, \tag{3.14}$$

where A_{prim} denotes the area of the primitive surface cell. Since the computational effort involved in obtaining the total energies in Eq. (3.11) can be significant, only rather small sets of surface phases can realistically be considered in minimizing Eq. (3.13).

When $\mathscr{E}_{\text{ads}}$ has been obtained for each such surface phase, the relative chemical potential can be varied as a parameter to obtain a set of $\Delta\gamma_{\text{ads}}$-lines. The convex hull of this set of lines then provides a compact way of representing what surface phase is the most stable for a given value of the chemical potential.

Further information can be obtained once the source has been fully specified. For instance, assuming an ideal gas of X molecules, the activity equals the pressure and

$$\mu_X(T,p) = \mu_X^\circ(T,p^\circ) + k_B T \log\left(\frac{p}{p^\circ}\right), \tag{3.15}$$

where the reference state is typically taken at $P^\circ = 1\,\text{atm}$. Accordingly, the relative chemical potential is

$$\Delta\mu_X(T,p) = \left(\mu_X^\circ(T,p^\circ) - E_X - \mu_X^{\text{vib}}(T)\right) + k_B T \log\left(\frac{p}{p^\circ}\right), \tag{3.16}$$

and inside the parentheses on the right-hand side of this equation, only the translational, rotational and configurational contributions to the free energy will remain after the subtractions. If configurational contributions are neglected, all other terms can be evaluated from simple analytical expressions [52]. By fixing either the temperature or the pressure, the relation $\Delta\mu_X = \Delta\mu_X(T,p)$ can be inverted to obtain a corresponding range of the other variable.

The phase stability construction prescribed by Eqs. (3.9) and (3.13) was employed in **Paper I** to investigate the phase stability of gas-phase alkanethiolates adsorbing on the Au{111} surface in ultra high vacuum. When the alkyl chain is short, only two phases exists: the clean surface and a high coverage monolayer of thiolates (Fig. 3.2a). For longer alkyl chain, however, an additional low coverage phase appears where the thiols adopt a lying-down configuration to maximize their dispersive interactions with the surface (Fig. 3.2b). Equation (3.16) was used to correlate values of the gas-phase chemical potential with temperatures to enable comparison with experimental data from temperature programmed desorption measurements.

3.2 Equilibrium shapes of nanoparticles

If the surface free energies of different facets are known the thermodynamic equilibrium shape of a nanoparticle can be obtained by means of the *Wulff construction* [53]. Consider a surface consisting of facets $\left\{(h_i k_i l_i)\right\}_{i=1,2,\ldots}$ with associated surface free energies $\gamma^i \equiv \gamma^{h_i k_i l_i}$, areas A_i, and distances to the crystal center h_i. The total volume of the particle is given by

$$V = \sum_i \frac{1}{3} h_i A_i. \tag{3.17}$$

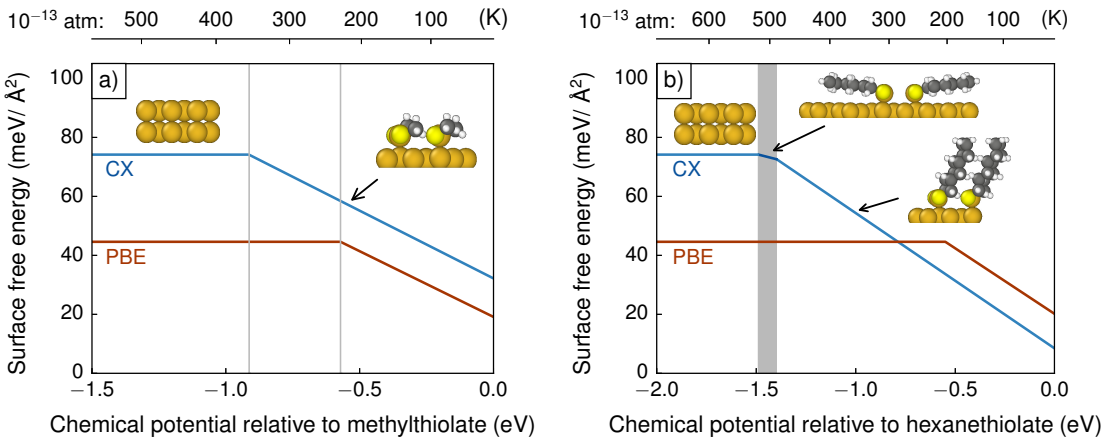

Figure 3.2: Phase stability curves for adsorption of gas-phase alkanethiolates on gold as a function of either the relative chemical potential of the adsorbates or, assuming ultra high vacuum conditions, the temperature. a) For methylthiolates only the clean surface and a dense monolayer are stable. b) For hexanethiolates an intermediate phase is also found where the alkyl chains are almost perpendicular to the surface due to dispersive interactions.

The total free energy of the particle can be decomposed into contributions from the bulk and the surface

$$G = G_{\text{bulk}} + G_{\text{surf}} = G_{\text{bulk}} + \sum_i \gamma^i A_i. \tag{3.18}$$

The equilibrium shape of a particle can be found be minimizing G under the constraint of constant volume, introduced through a Lagrange multiplier [54].

$$\delta(G - \lambda V) = \delta G_{\text{bulk}} + \sum_i \delta\left(\gamma^i A_i - \frac{\lambda}{3} h_i A_i\right) = 0. \tag{3.19}$$

In the above equation the first term vanishes since the volume is fixed and consequently the variation can only vanish if the terms in the summation independently vanish. This proves the Gibbs-Wulff theorem

$$h_i = \text{const.} \times \gamma^i. \tag{3.20}$$

A Wulff construction is a polar plot of the surface tension as a function of orientation $\gamma^{\hat{\boldsymbol{n}}}$ with $\hat{\boldsymbol{n}}$ lying in the unit sphere $\mathcal{S}^3$. The Gibbs-Wulff theorem then guarantees that the equilibrium shape, or *Wulff shape*, can be obtained from the Wulff construction as the

convex hull of the set of planes defined by having surface normals $\hat{\boldsymbol{n}} \in \mathcal{S}^3$ at distance $\gamma^{\hat{\boldsymbol{n}}}$ away from the crystal center.

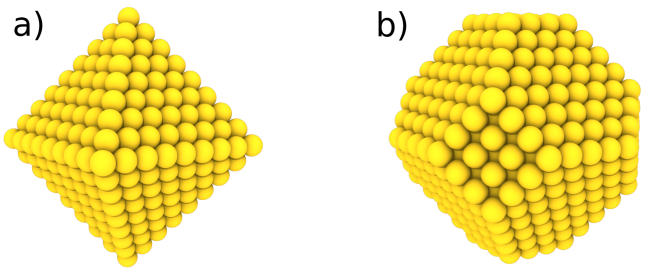

Figure 3.3: Examples of single-crystalline nanoparticle shapes for fcc metals. a) An octahedron exposes only energetically favorable {111} facets but is very aspehrical. b) A Wulff construction shows that the stable shape for this volume is the derived regular truncated octaderon, where the corners of an octahedron have been truncated to increse the sphericity.

As an illustration, consider the equilibrium shape of a gold nanoparticle in vacuum. For fcc metals such as gold the low-index facets follow the energetic ordering $\{111\} < \{100\} < \{110\}$, which derives from the reverse ordering of the surface atom coordination numbers. It could thus be conceived that the most stable shape would be an octahedron (Fig. 3.3a) that exposes only {111} facets. This is not the case, however, since the asphericity of the octahedron carries a high energy penalty. A Wulff construction reveals that the stable shape is a regular truncated octahedron (RTO) (Fig. 3.3b), where a more spherical shape is assumed by truncating the corners of the octahedron to expose {100} facets as well.

The Wulff construction is not limited to nanoparticles with clean surfaces in vacuum, adsorbates and the chemical environment can be taken into account by calculating surface free energies γ^i from Eq. (3.9). In this way the faceting of the particle is obtained as a function of the relative chemical potential of the adsorbates, which can subsequently be related to experiment. The Wulff construction has, however, many deficiencies. First, it provides no atomic resolution and hence only equilibrium shapes corresponding to certain sets of so-called *magic numbers* of atoms can be obtained since atoms have to be added layer by layer. Second, the effect of corners and edges is also lost, which especially constitutes a limitation for smaller particles where the relative fraction of atoms occupying such sites is large. Lastly, strained, poly-crystalline geometries such as icosahedra and decahedra are precluded. Recently, a different method for nanoparticle construction via variance constrained semigrand-canonical [55] Monte Carlo simulations has been developed that overcomes these two difficulties [56]. This proves useful in the context of analyzing the structure of gold seeds used in the synthesis of nanorods, where twinned structures are commonly observed (Sect. 2.3, Sect. 4.3).

4

Understanding seed-mediated growth of gold nanorods

"You know the detective's curse?" The solution was right under my nose but I was paying attention to the wrong clues.

Martin "Marty" Hart

Understanding nanoparticle growth from solution is, in general, a non-trivial problem due to the complexity of the interactions and the mechanisms involved. This results in a system governed by processes that occur over vastly different time and length scales, making theoretical as well as experimental analysis difficult. This is in particular true for the growth of anisotropic nanoparticles using seed-mediated growth protocols, which involves an additional growth stage after synthesis of the seeds where further reagents are introduced into an already complicated system (Sect. 2.3).

Yet, a detailed theoretical understanding of the mechanisms that control anisotropic nanoparticle growth is of paramount importance for the systematic improvement of existing synthesis protocols, and will in turn enable many potential applications that rely on access to large quantities of nanoparticles with tailored properties. With this goal in mind, a reasonable approach is to focus on a particular system and explore to which extent the results may be generalized to other instances of seeded growth protocols. The synthesis of gold nanorods (AuNR) constitutes an ideal candidate since there is a plethora of interesting applications based on their plasmonic properties, a large body of experimental work already published on the topic, and many open questions surrounding the growth mechanism [57, 37].

The current chapter serves as an exposition of several aspects important to understanding the growth process and aims at providing a stepping stone towards a compre-

hensive picture of AuNR seeded growth. The ideas developed are based on combination of work carried out by the author and the Computational Materials group at Chalmers. A critical review of growth models put forth in the literature is also presented.

4.1 Aspects of gold nanorod growth

To systematically analyze the synthesis of gold nanorods, the first step is the identification of several key aspects of the growth. This is accomplished through a decomposition of the growth process into different temporal and spatial regions (Fig. 4.1). The first aspect (**A-1**) concerns the structure of the seed particles and extends temporally from the beginning of the seed solution synthesis until right before the seeds are injected into the growth solution. The remaining three aspects separate the subsequent anisotropic growth into three spatial regions: the chemistry of the growth solution (**A-2**), the structure of the surfactant layer (**A-3**) and the processes occurring at the gold surface (**A-4**). Only **A-1** and **A-3** are treated in this thesis, apart from certain elements of **A-2** that emerge as a natural part of the discussion.

The fundamental question of **A-1** is the crystalline structure of the seed particles and their impact on the subsequent growth into nanorods. This necessitates the subproblem to also encompass adsorbate related effects such as the altering of surface energetics. Despite the labeling, it is discussed after **A-3** for reasons that will become apparent presently. As alluded to in Sect. 2.2.1, CTAB is often attributed the role of shape directing agent in AuNR synthesis and the veracity of this statement is the central theme of **A-3**. More precisely, this aspect covers the geometry of the surfactant layer after the growth solution has been added as well as related processes such as diffusion of monomers to the surface. **A-2** deals with reactions occurring in the bulk solution, where the chemical composition of the gold-containing compounds is the central question. Lastly, **A-4** addresses processes occurring at the metal surface such as reduction of gold ions and diffusion.

4.2 The surfactant layer (A-1)

One of the ideas underpinning the introduction of the **P-1** protocol was that CTAB could act as a shape-directing agent, encouraging growth of isotropic seeds into rods [26]. This interpretation was supported by the observation that in the absence of micelle forming surfactants, a similar seeded growth method could yield only a small fraction of rods in an unreliable manner [58]. Subsequent work explored the impact of seeds [59], surfactant [60] as well as synthesis conditions [61] on rod growth. Of particular significance was the observation that both the nature of the head group and length of the alkyl chain are crucial for obtaining nanorods. Indeed, substituting C_{16}TAB for

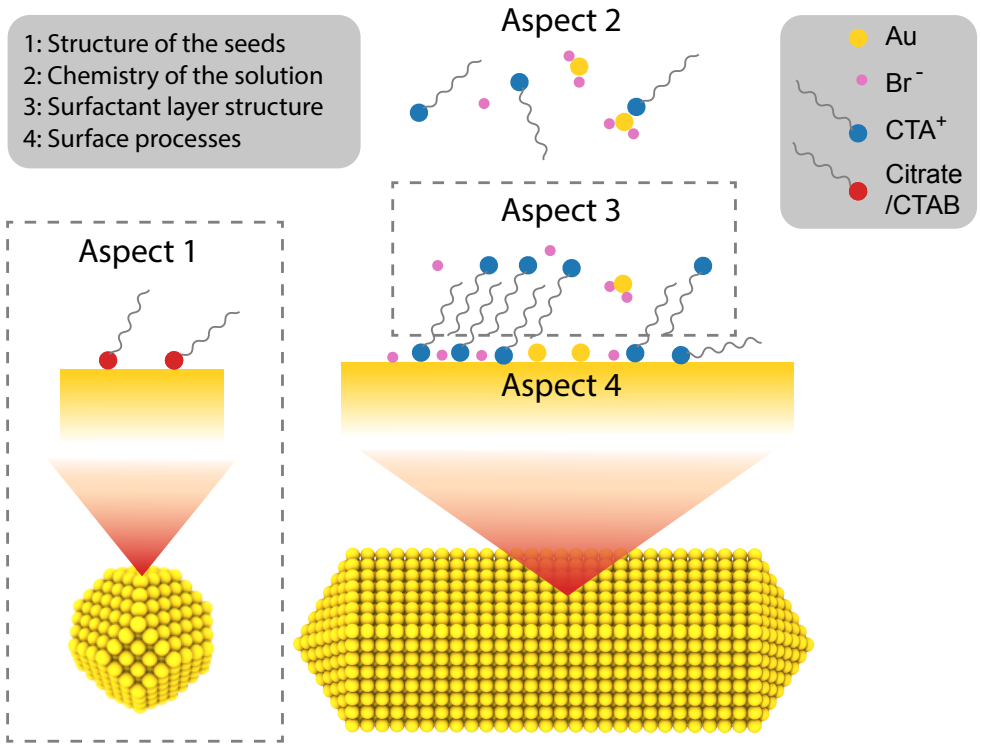

Figure 4.1: As a convenient analysis tool, the gold nanorod growth process is partitioned into a set of key aspects. **A-1**) The structure of the seeds: how it is determined and how it affects the growth. **A-2**) The chemistry of the bulk solution: reactions and chemical composition of gold-containing compounds. **A-3**) The surfactant layer and its role as a shape-directing agent. **A-4**) Processes occurring at the surface: reduction of gold ions and diffusion.

C_{16}PC (hexadecyl phosphorylcholine) produces no rods at all while going from C_{10}TAB to C_{16}TAB leads to an almost linear increase in aspect ratio from about 2 to 25 [60]. The search range for surfactants viable for rod growths has since been greatly expanded, confirming the prominent position occupied by CTAB in nanorod synthesis [62]. The wealth of experimental data uncovered by the studies in the early 2000's served as a basis for the first rudimentary model aimed at explaining the **P-1** growth as outlined below.

Bilayer blocking (M-1). The model invokes preferential adsorption of CTAB at certain crystallographic facets in order to explain how anisotropic growth can be sustained. More precisely, the model suggests that it is favorable for CTAB to adsorb on the {100} prism facets to form dense bilayers, which block incoming monomers from reaching

the underlying surface. In contrast, the rod terminations remain open for monomers (Fig. 4.2) and hence growth on the pyramidal facets is templated. Since shorter alkyl chains imply less stable bilayers that are more are likely to allow monomers to reach the metal surface, the observed increase of rod AR with increasing alkyl chain length is accounted for. It is also suggested, that due to the significant vdW interactions between alkyl chains, the bilayers can spill over the prism facet edges. As a result, incoming monomers are guided towards the terminations, further encouraging growth in a process reminiscent of a ziplock.

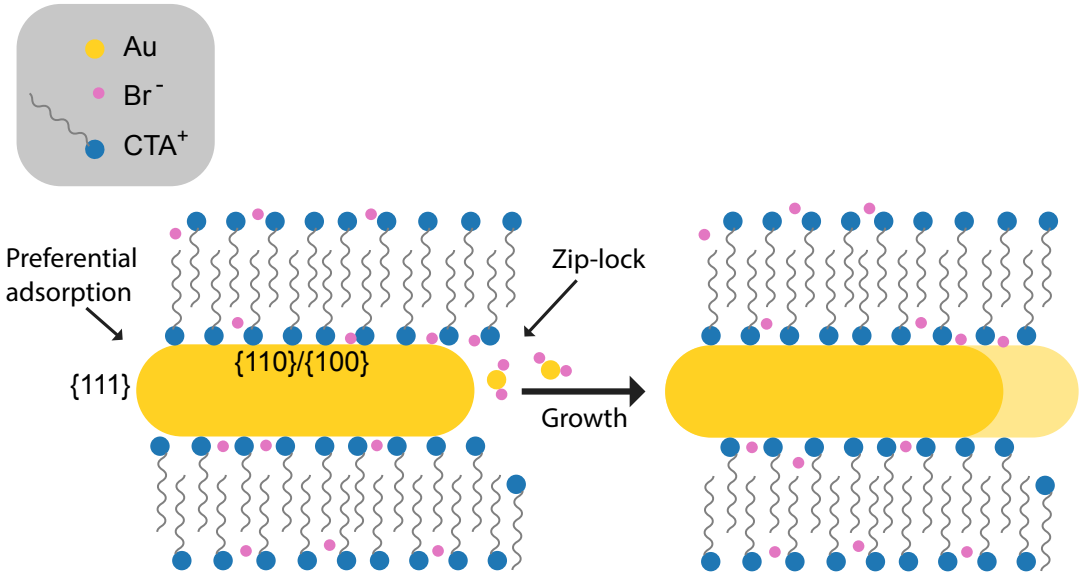

Figure 4.2: Conceptual "bilayer blocking" model for gold nanorod growth. Preferential adsorption of CTAB on the prism facets leads to formation of bilayers that block growth on these facets. On the terminations pyramidal facets are open for growth and bilayers spilling over the prism facet edges provide additional guidance for incoming monomers.

There are several shortcomings with **M-1**, most notably the lack of mechanistic details. For example, there is no clear statement about the state of the surfactant layer on the pyramidal facets. Since CTAB adsorption is exothermic on Au{111} [62] it cannot be excluded that at some point during the growth these facets develop the capability to support a micellar structure. If a bilayer forms, it is unlikely that the negatively charged complexes carrying Au-ions are able to reach the surface, given that similar structures such as phospholipid bilayers are known to be impermeable to ions [63]. It is also important to note that while preferential adsorption and blocking of facets by CTAB will inevitably lead to anisotropy, growth into rods is not guaranteed. The final shape of the

nanoparticles would in this picture largely be determined by the faceting of the seeds and their evolution in the early moments after the growth solution is added (Sect. 4.3).

The picture of adsorbed CTAB molecules forming a bilayer on the gold surface pervades the AuNR literature. It is motivated by experimental measurements [64, 65, 66] of composition, thickness and density of the surfactant structure, which are consistent with a bilayer. In particular the observed thicknesses fall in the range $32 - 39$ Å, corresponding to partially interdigitated alkyl chains (Fig. 4.2). An essential consideration that is often missing, however, is the surface phase behavior of CTAB; there are no *a priori* reasons to assume that the surfactant layer is confined to a single phase as the CTAB concentration changes, or that other phases would affect the growth in the same way as a bilayer. The phase behavior of the related system of CTAB on a silica surface testifies to this claim, as shown in a study by Kadirov et al. [67]. The silica surface was imaged and the local topography probed with liquid atomic force microscopy (AFM) at different CTAB concentrations.

Combining this data with electronic spin resonance (ESR) measurements, a one-dimensional surface phase diagram was proposed as a function of the bulk CTAB concentration (Fig. 4.3). Note that the concentrations used here (~1 mM) are much lower than what is normally used in seed-mediated growth protocols (~100 mM). In this system, the first phase with long-range order is a bilayer, which is quickly superseded by cylindrical and spherical micellar phases as the concentration increases. The presence of these latter phases can be of importance for understanding growth phenomena, since they differ from the bilayer in terms of how accessible the underlying surface is to incident monomers.

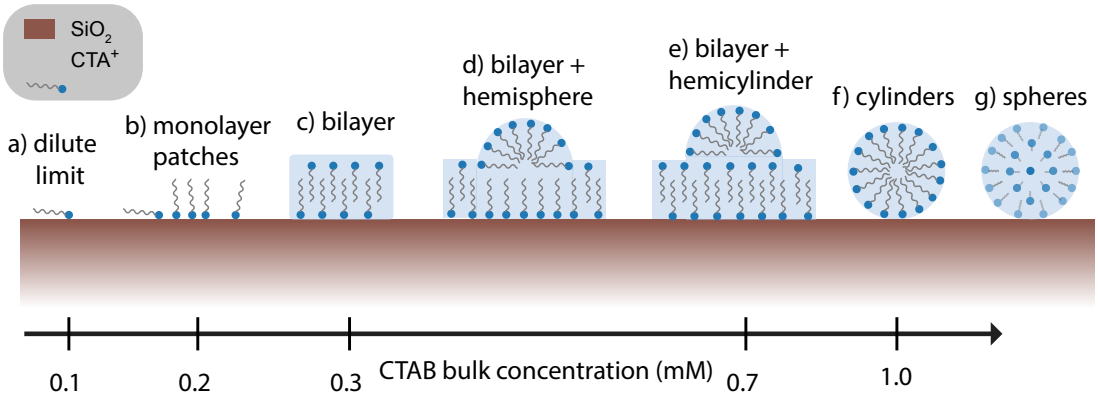

Figure 4.3: One-dimensional Phase diagram of CTAB on a silica surface as a function of CTAB concentration, deduced from a combination of ESR and AFM measurements [67]. At intermediate concentrations, the underlying silica substrate is blocked by a bilayer until the appearance of cylindrical and spherical micelle phases at higher concentrations.

The idea of cylindrical CTAB micelles as a driving force for gold nanorod growth has been proposed by Meena and Sulpizi [68]. They employed force-field molecular dynamics (MD) simulations to study CTAB adsorption on the three low-index surfaces {111}, {100} and {110} of gold under aqueous conditions. The key observation was that a CTAB surfactant layer initialized in the form of a dense bilayer collapses into a distorted cylindrical micelle (Fig. 4.4). Consequently, *channels* are formed between neighboring cylindrical micelles with widths between 0.7 nm and 1.0 nm. The channels thus provide room for monomers from the bulk solution to diffuse through the surfactant layer region and reach the surface (Fig. 4.4). Furthermore, the width of channels found on the {111} surface is greater than on {100} and {110} (Table 4.1). It was concluded that this causes a difference in the arrival rate of monomers to the surface which could potentially explain the anisotropy required for nanorod growth, since in **P-1** rods expose {100} prism facets and {111} pyramidal facets on the terminations (Fig. 2.5). Furthermore, the plane-averaged charge distribution (Fig. 4.5a) shows a slight enrichment of bromide relative to nitrogen at the surface, which is overcompensated by a larger excess of nitrogen relative to bromide in the interfacial region between the micelle and the bulk solution. As a result, the micelle acquires a net positive charge and an electric potential drop is experienced by negative species passing through the channel towards the surface (Fig. 4.5b). The magnitude of this potential difference is facet-dependent and attains a maximum for the {111} surface (Table 4.1), possibly contributing further to an anisotropic growth rate.

The work by Meena and Sulpizi was later extended to changes to the micellar structure in going from infinite surfaces to finite facets on decahedral and cuboctahedral seeds around 5 nm [69]. It was found that cylindrical micellar phases develop on {100} and {110} facets, while no adsorption takes place on {111}. The subsequent conclusion was that, in this way, a large propensity for anisotropy could develop during the early stages of growth. Some skepticism is warranted here since these calculations assumed, without motivation, a decahedral seed with very elongated {100} facets (see the discussion in Sect. 4.3 for more details).

Halide substitutions to the headgroup of CTAB were also investigated [70], revealing that, for instance, partially replacing Br^- with Cl^- loosens the micellar structure, leading to a collapse of the channels when the concentration of chloride relative to bromide is sufficiently high. As exemplified by these simulations, a model based on the surfactant layer structure could be used to understand many other experimental observations in addition to the monomer transport.

In contrast to **M-1**, the above picture of growth based on channels provides a sensible mechanism for diffusion of monomers to the surface. It cannot, however, be stated without further investigation that the differences in channel width and potential drop between different facets alone yield monomer arrival rates that fully explain the anisotropy of the facet growth rates. Even more problematic, Meena and Sulpizi only reported their findings for a single value of the CTAB surface density. No argu-

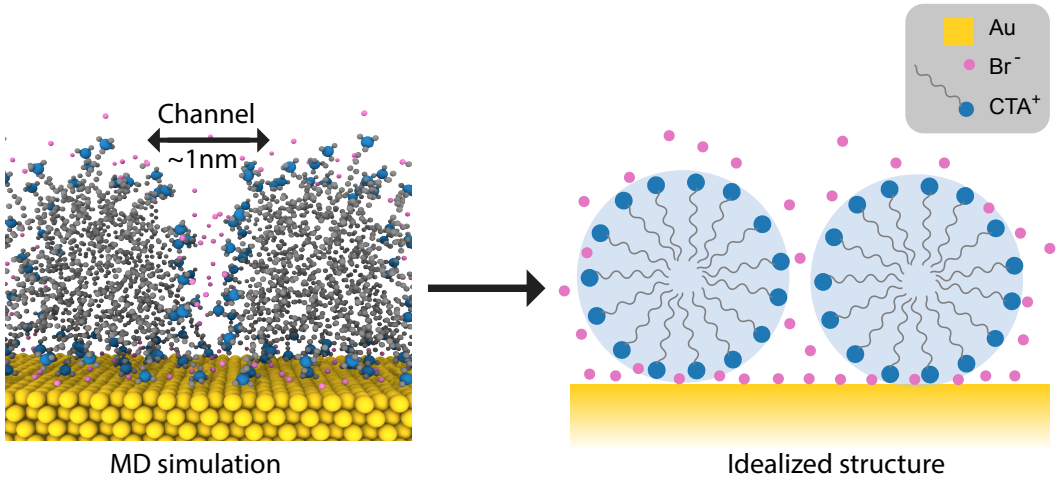

Figure 4.4: Left: a snapshot from the an MD simulation of CTAB on Au{111} showing the formation of a channel between two distorted cylindrical micelle. Right: idealized cylindrical structure derived from the MD simulation. Here, CTAB headgroups are represented by an effective cation (blue).

Table 4.1: Width and potential drop along channels formed by cylindrical CTAB micelles on low-index gold surfaces. Both properties are facet-dependent and possibly contribute to the anisotropic growth of gold nanorods. Data from Meena et al. [68].

Surface	Channel width (nm)	Potential drop (V)
Au{111}	0.94	0.80
Au{100}	0.73	0.68
Au{110}	0.71	0.70

ment was made for how this density can be related to the bulk concentration, which can be controlled and measured experimentally, and hence no definite conclusions can be drawn regarding the growth mechanism. Conceivably, the channels could disappear in the true experimental density range, or exhibit either a weak or non-existing facet-dependence. This would certainly invalidate any model where the channels are responsible for the sustained anisotropic growth, and establishing a surface phase diagram is therefore of utmost importance. This line of investigation is currently being pursued in our research group, employing a combination MD simulations[1] with the same force field setup as used in [68] and DFT calculations.

In the MD simulations, the phase diagram can be explored by varying the surface

[1]performed by Narjes Khosravian

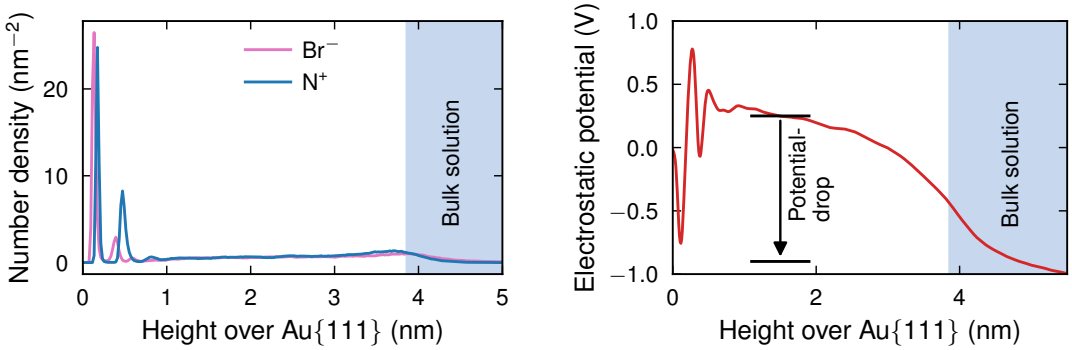

Figure 4.5: a) Number densities of bromide ions and nitrogen along the channels. For illustrative purposes nitrogen is labeled as a cation although the charge is spread out over the CTA headgroup. An uncompensated excess of nitrogen in the interfacial region between surfactant layer and bulk solution interface gives leads to a net positive charging of the micelles. b) The charge distribution gives rise an electrostatic potential drop along the channel, which drives anions towards the surface.

packing density η_s, defined as the number CTAB molecules adsorbed on, or otherwise positioned in the proximity of, the surface per area unit. Before turning to the quantitative results, it is instructive to look at a qualitative sketch of the obtained phase diagram (Fig. 4.6). Currently, simulations for a wide range of η_s values are only available for CTAB on Au{111}. Figure 4.6 reveals a phase behavior that bears many similarities to that of CTAB on a silica surface (Fig. 4.3). In general, understanding the driving forces behind phase transitions in self-assembled surface systems is non-trivial; minimization of the free energy requires striking a balance between entropy and enthalpy, where the enthalpy alone will receive a long list of contributions. These come predominantly from molecule-molecule (Sect. 2.5.2), surface-molecule (chemisorption, vdW) and solvent-molecule (hydrophobic and solvation) interactions. For the first few phases in Fig. 4.6, where the η_s is low, however, much of the behavior can be understood in terms of maximizing the vdW interactions that are present between two alkyl chains (chain-chain) and between an alkyl chain and the surface (chain-surface). In **Paper I**, these effects are studied for a thiolated Au{111} surface, a system that is frequently used as a prototype for self-assembly at metallic surfaces, using dispersion-corrected density functional theory (Sect. 5.2). It is found that for molecules with an alkyl chain adsorbed on a gold surface, there can be thermodynamically stable phases where the thiols are lying flat against the surface (Fig. 3.2). At higher packing densities, transitions to standing-up phases can then arise from a competition between chain-chain, chain-surface and steric interactions. More precisely, the surface-chain interactions scale as 0.07 eV/CH_2 compared to 0.05 eV/CH_2 for the chain-chain interactions [71]. This implies that, for longer alkyl chains the system can tolerate more unfavorable steric interactions as thiols are

added before a transition to a standing up phase occurs.

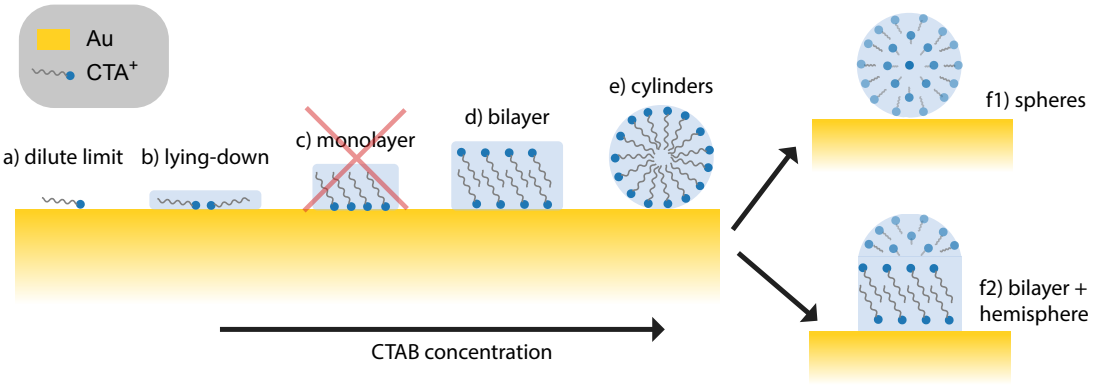

Figure 4.6: Qualitative phase diagram for CTAB on Au{111} determined from force-field based MD simulations. At low concentrations, a lying-down phase presides due to strong interactions between the surface and alkyl chains. A surface blocking bilayer is then obtained as the concentrations increases. At high concentrations cylindrical micelles featuring channels appear, followed by either a hemispherically capped bilayer or spherical micelles.

Returning to the phase diagram of CTAB on gold with these results in mind, it is unsurprising that the MD simulations reveal that CTAB under dilute conditions adopts lying-down configurations where the vdW-interaction with the surface are maximized (Fig. 4.6a,b). In the intermediate packing density range, a bilayer (Fig. 4.6d) is directly formed without first passing through a monolayer phase (Fig. 4.6c). The absence of a monolayer can also be rationalized in terms of the CTAB alkyl chain and the aforementioned scaling of the vdW interactions. Due to the size of the headgroup, CTAB molecules in a standing-up monolayer phase cannot achieve sufficient stabilization from vdW interactions, and as the density increases the bilayer phase is immediately nucleated (Sect. 2.6) from the lying-down phase. For high values of η_s, the bilayer is eventually replaced by cylindrical micelles featuring channels as observed by Meena and Sulpizi. The cylindrical micelles can be followed by another bilayer phase capped with hemispheres (Fig. 4.6e,f2) or spherical micelles (Fig. 4.6e,f1) depending on the initial configuration of the MD simulation (see discussion below).

A more detailed interpretation of the MD data for the phase diagram requires an understanding of the role of the initial configurations used in the simulations. Here, it was found that the most convenient choice is a bilayer superlattice, which allows for the surface packing density η_s to be controlled in a systematic manner by changing the lattice constant. Another important parameter turns out to be the level of interdigitation of the alkyl chains in the starting bilayer. Letting η_s range over $[1.2, 3.0]$ nm^{-2}

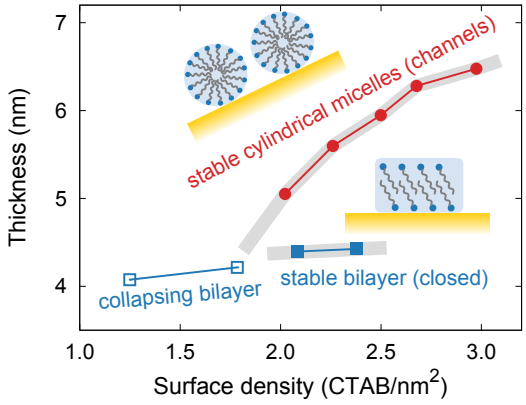

Figure 4.7: Quantitative phase diagram for CTAB on Au{111} determined from force-field based MD simulations. Different phases are obtained depending on the surface packing density of the initial configuration and the interdigitation of the alkyl chains. The general trend is that the system goes from a bilayer to cylindrical micelles and finally to a hemispherically capped bilayer or spherical micelles (not shown). Large overlap regions between these phases occur due to kinetic trapping.

and assuming either high or no interdigitation for each η_s reveals that in certain parts of this density range, the interdigitation determines what phase systems ends up in (Fig. 4.7. In the lower part of the range $\eta_s \in [1.2, 1.8]\,\mathrm{nm}^{-2}$, the bilayer is unstable and quickly collapses as the packing is not dense enough for chain-chain interactions to uphold the molecules. This structure is subsequently followed at intermediate values $\eta_s \in [1.8, 2.5]\,\mathrm{nm}^{-2}$ by an overlap region where a starting configuration with high interdigitation leads to a stable bilayer and a configuration with no interdigitation at all yields cylindrical micelles. The existence of the overlap region suggests that either the free energy barrier towards cylinder formation is high enough to kinetically trap the system in a bilayer phase, or that the bilayer is indeed more stable in this η_s-range. If the latter is true, then there is a corresponding barrier preventing a cylindrical micelle from turning into a bilayer. Currently, these two situations cannot be distinguished in the MD simulations. For $\eta_s > 2.5\,\mathrm{nm}^{-2}$ initial configurations starting from interlocked bilayers are no longer stable and the high density causes molecules to be partially expelled from the bilayer into the solution. Non-interlocking bilayers, on the other hand, still turn into stable cylinder up to $\eta_s = 3.0\,\mathrm{nm}^{-2}$. It is also possible for $\eta_s > 2.7\,\mathrm{nm}^{-2}$ to obtain spherical micelles (not included in Fig. 4.7) from more disordered bilayers with no interlocking. For the configurations used to obtain cylindrical micelles, however, a hemispherically capped bilayer takes over when $\eta_s > 3.0\,\mathrm{nm}^{-2}$.

As discussed, the relative stability of phases with overlapping ranges is hard to de-

termine, judging by the silica phase diagram (Fig. 4.3) a phase consisting of spherical micelles would have been expected given the high CTAB concentrations used in seed-mediated growth protocols. It is possible that due to kinetics, the probability of forming a spherical micelle without first passing through an intermediate cylindrical shape is extremely low, putting the spherical phase out of reach for the MD simulation which for practical purposes is effectively constrained to always start from a bilayer-like structure.

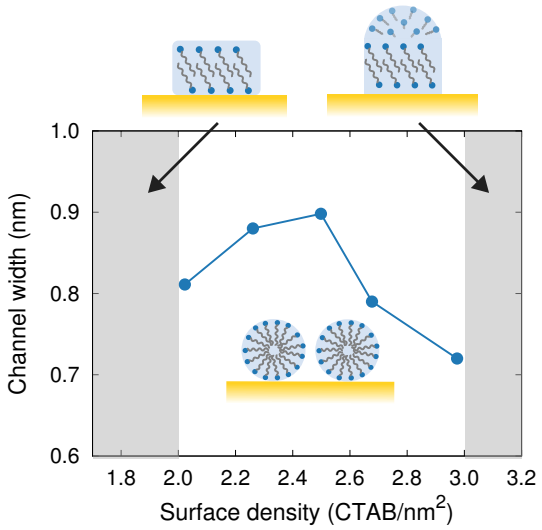

Figure 4.8: Channel width of cylindrical CTAB micelles on Au{111} determined from force-field based MD simulations. The width varies with the surface number density and displays and peaks at intermediate densities. The channels subsequently close at the onset of the hemispherically capped phase. The relevance of this phase is hard to gauge as there exists also a spherical micelle phase at high packing density which is permeable but difficult to reach in the MD simulation due to kinetics.

The surface phase diagram outlined above has many implications for nanorod growth. One consequence is that the time-averaged channel width $\langle w \rangle$ of the cylinders varies with the surface number density (Fig. 4.8). A peak value of $\langle w \rangle = 0.9$ nm of is exhibited around $n_s = 2.5\,\mathrm{nm}^{-2}$. Beyond this point, the width successively falls off to 0.7 nm on the approach to the hemispherically capped bilayer phase and the accompanied closing of the channels. The notion of an upper limit to the packing density range corresponding to growth is not very appealing in the light of the very high CTAB concentrations that are used in the **P-1** and **P-2** protocols. In the absence of a relation between the bulk CTAB concentration and the surface packing density, however, no definite comparison can be made. Packing densities in Fig. 4.7 generally corresponds to concentration on the order of 1 M in a volume close to the surface, which is one order of magnitude

higher than the 0.1 M used in the **P-1** protocol. Since CTAB chemisorbs to the surface this is only provides an upper bound and hence the experimental concentration could correspond to any part of the range in Fig. 4.7. As noted in the preceding paragraph, it is very likely that a phase consisting of spherical micelles exists a higher packing densities might be hard to reach in the MD simulation. If this phase is more stable than the hemispherically capped bilayer, it would mean that beyond the cylindrical micelle region an even more permeable phase is present Fig. 4.8.

Regarding the anisotropy of the facet growth rates, care should be taken to distinguish between the origin of the anisotropy and the how it is subsequently sustained during the growth since there may be different, complementary mechanisms involved. Unfortunately, full phase diagrams for the {100} and {110} surfaces have not yet been determined, but preliminary simulations at several selected packing densities indicate no clear trend in the facet-dependence of $\langle w \rangle$. That is to say, while similar values as reported in Table 4.1 may be obtained a specific packing density, the trend can be broken in going to higher or lower values. Furthermore, the channels fluctuate with time, giving rise to oscialltions of the width by about 0.2 nm in magnitude, which is very similar to the difference in $\langle w \rangle$ between the facets. In conclusion, it seems unlikely that a facet-dependent channel width could explain the sustained anisotropic growth. There is still the possibility that facet-dependence of the potential drop could emerge as a clear trend at different densities, but sufficient data has not yet been gathered to either confirm or disprove this.

Allowing for some speculation, a different mechanism for generating anisotropy could be conceived in the form of a facet-dependent phase diagram, where the packing density corresponding to a transition from a phase A to B is different for the three low-index facets. A facet-dependence of this sort could come about for several reasons, e.g., due to stronger binding of CTAB on the more open {100} and {110} facets.

As a means of summarizing the above findings and discussion, a tentative growth model is presented below.

Phase model (M-2). This model describes the mechanism of gold nanorod growth in the **P-1** protocol in terms of the phase diagram of CTAB on gold. A truncated decahedral seed particle with slightly elongated {100} facets is assumed (see Sect. 4.3). Upon addition of the seeds to the growth solution, CTAB starts to adsorb and form micelles which, at first, develop primarily on the prism facets, as the {111} patches are still too small to support micelles. This templates anisotropic growth until the point where micelles start forming also on the terminations. Initially bilayers are formed that subsequently transition to either cylindrical or spherical micelles to allow monomers to reach the surface. The latter process is facilitated by the positively charged micelles and associated potential drop along the channels. Anisotropic growth is sustained by either a facet-dependence of this micellar charging, or a facet-dependence of phase transition

points. The second option could, for instance, be realized by a surfactant layer on the prism facets remaining (trapped) in a bilayer phase due to stronger binding of CTAB on these facets.

4.3 Structure of the seed particles (A-2)

The models for AuNR growth described in Sect. 4.2 invoke, in one way or another, an asymmetry between {111} and the two other low-index facets {100} and {110} to explain the anisotropic growth. This will, however, only lead to a nanorod if the initial seed particles have the right faceting, either before their injection into the growth solution or shortly thereafter. Consider, for example, a cuboctahedral seed (Fig. 4.9d), which is obtained by taking a cubic particle with six {100} facets and truncating the corners to expose eight {111} facets. With anisotropic growth rates as prescribed above this would simply grow into a cube. In addition, AuNRs synthesized using in the **P-1** protocol have a penta-twinned structure (Fig. 2.5). In order to find a shape that could grow into a nanorod, it is thus logical to start by considering seed shapes that have five-fold twinning. The ideal candidate is a truncated decahedron (Dh) (Fig. 4.9a), which is simply a penta-twinned nanorod where the prism facets are not elongated.

The next question is what structures dominate the shape distributions obtained from the seed synthesis. From a theoretical point of view, the equilibrium shape of a nanoparticle can obtained from a Wulff construction (Sect. 3.2), which requires as input a set of facets and their associated surface energies. The chemical environment, including adsorbates, finite temperature etc. can then be incorporated into a Wulff construction by using an ab initio thermodynamics model (Sect. 3.1). The issue with this approach is that the conventional Wulff construction does not take into account the strain inherent in a twinned structure or the energy associated with the twin boundary.[2] Consequently, a decahedral nanoparticle cannot correspond to a Wulff shape.

As discussed briefly in Sect. 3.2, another approach is offered by Rahm and Erhart [56], where the equilibrium shape can be obtained for an arbitrary number of atoms, in contrast to the Wulff construction, which only generates particles corresponding to magic numbers. Furthermore, the method has atomic resolution and hence strain and twin-planes are accounted for. Using this approach Rahm and Erhart determined the equilibrium structure of an isolated, clean, gold nanoparticle in vacuum for particles with diameters up to 7 nm. The results show that for diameters around 5 nm relevant for AuNP seeds, equilibrium shapes are distributed almost evenly between decahedral and octahedral motifs. The shapes that feature most predominantly is the Marks decahedron (MDh) (Fig. 4.9c) and the regular truncated octahedron (RTO) (Fig. 4.9d). Here, the MDh is a special version of a truncated Dh that introduces re-entrant surfaces at the

[2] A stable decahedron offsets the penalty from these effects by exposing more {111} surface.

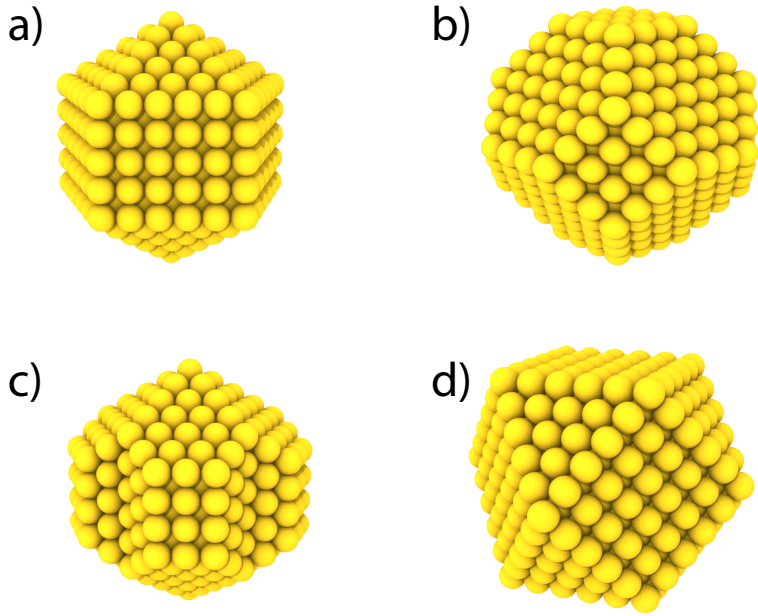

Figure 4.9: Various nanoparticle shapes relevant for AuNR seed-mediated growth protocols. a) Truncated decahedron: candidate seed shape for growth into penta-twinned nanorods. b) Regular truncated octahedron: typically favorable for larger nanoparticles in vacuum. c) Marks decahedron: generally preferred over the truncated decahedron and stable for smaller nanoparticles in vacuum. d) Cuboctahedron: the dominant seed shape in the **P-2** protocol.

corners. The RTO is derived from an octahedron that exposes only energetically favorable {111} facets, but is generally not stable due to the sharp corners. The RTO lowers the energy of its parent shape by truncating the corners, thereby revealing also {100} facets. In contrast to the Dh, the RTO is single-crystalline. It should be noted that in obtaining these results an embedded-atom model potential fitted to density functional theory data based on the PBE functional (Sect. 5.2.3) was used to calculate energies of different particle configurations needed by the algorithm. Since PBE does not produce accurate surface energies for fcc transition metal, [72], the results in [56] should be taken to indicate a trend rather than as a source of quantitative data.[3] Nevertheless, this work shows that in vacuum, a significant portion of gold seeds would assume a decahedral structure. Unfortunately, incorporating the effect of the chemical environment into this approach does not seem to be straightforward[4].

[3]This would require using a potential fitted to data generated from a functional that produces more accurate surface energies. Here, vdW-DF-cx is a promising candidate (see **Paper I**).

[4]Magnus Rahm, (personal communication, September 13, 2017)

Experimentally, there is evidence that a portion of the seeds are indeed decahedral under **P-1** synthesis conditions [73], lending credence to the claim that it is these seeds that grow into rods. This does not explain the origin of the anisotropic growth, however, since for the shapes predicted by Rahm and Erhart, the MDh particles do not exhibit elongated {100} facets. Instead, {111} facets occupy the largest fraction of the surface area and consequently, there must exist a mechanism for face-selectivity for elongated Dh seeds to be obtained. A possible explanation could be a stabilization of {100} relative to {111} due to adsorption of citrate, which is the capping agent used in the **P-1** protocol. To convincingly test this hypothesis, an extension of the Wulff construction capable of describing twinned particles [74] in conjunction with an ab initio thermodynamics model. A comparison could then also be made to the **P-2** synthesis, which is known to produce single-crystalline nanorods from seeds that are predominantly single-crystalline as well [75]. Since the only difference between the two protocols with respect to the seed synthesis is the stabilizing agent used (citrate or CTAB), there is a lot of insight regarding the shape selectivity of the capping agents to be gained from such a study.

4.3.1 Growth mechanism

The underlying processes of the seed synthesis are not fully understood and indeed, the subsequent growth into rods is independent of the particular pathway taken during the seed formation insofar as the product seeds and the final chemical environment does not change. Hence, only a brief account of various mechanisms proposed in the literature will be given here.

Many studies of the underlying mechanism of AuNP growth have been conducted but the outcome as a whole remains indecisive. Some studies report that AuNP growth is adequately described by CNT coupled with diffusional growth [76] or Ostwald ripening [77], while others invoke non-classical pathways such as multi-phase nucleation [78]. Growth mechanisms for the classical Turkevich method as well as AuNP synthesis via fast $NaBH_4$ reduction in the absence of stabilizing agents have also been proposed by Polte and coworkers [79, 80] on the basis of in-situ investigations. In the latter case, which is relevant for the synthesis of AuNP seeds, the measurements revealed that the particle growth proceeds via the coalescence of successively larger gold clusters. Their results are rationalized by a picture markedly different from CNT. Since gold clusters consisting of just a small number of atoms are stable up to high temperatures under gas-phase conditions [81, 82], they argue that the free energy barrier for nucleation of a critical cluster (Eq. (2.23)) in solution under ambient conditions is effectively zero. It is then thermodynamically favorable for the small clusters to coalesce and form progressively bigger particles. The process is not halted until sufficient colloidal stability has been achieved, which occurs when the system encounters an energy barrier toward further coalescence and becomes kinetically trapped (Sect. 2.5). It must

be noted that no surfactant was used in this synthesis, however, a similar growth mechanism was identified [83] for a system of AgNPs reduced by $NaBH_4$ and stabilized by polyvinylpyrrolidone (PVP).

To summarize, current literature contains many, occasionally conflicting, interpretations of the mechanism behind AuNP growth. Further investigations are thus needed to clarify the issue and it must be considered that the particular pathway taken during a synthesis is likely very sensitive to the synthesis conditions. Care should also be taken when drawing on concepts from CNT since an increasing number of studies point to non-classical nucleation and growth mechanisms.

5

Methodology

5.1 First-principles calculations

"But, gentlemen, that's not physics."

Ceylonese parrot nominated as chairman for all seminars on quatum mechanics in Göttingen 1927.

All properties of a system of interacting, non-relativistic particles are in principle determined by its many-body state $|\Phi(t)\rangle$, which is obtained as a solution to the time-dependent Schrödinger equation

$$i\hbar\frac{\partial}{\partial t}|\Phi(t)\rangle = H|\Phi(t)\rangle\,, \tag{5.1}$$

where H is the Hamilton operator of the system. The spectrum of this operator, defined by the eigenvalue equation

$$H|\Psi\rangle = E|\Psi\rangle\,, \tag{5.2}$$

corresponds to the allowed energies E of the system. Equation (5.2) is often referred to as the time-independent Schrödinger equation. The eigenstates $|\Psi\rangle$ may be used as a basis for an expansion of an arbitrary many-body state, but for many applications it is sufficient to know the ground state of the system i.e. the lowest eigenvalue E_0 of H and its associated eigenstate $|\Psi_0\rangle$.

For a system consisting of N electrons and M atomic nuclei, the position-space representation of the Hamilton operator in Hartree atomic units ($\hbar = e = m_e = 4\pi\epsilon_0 = 1$) is given by

$$H = \overbrace{-\frac{1}{2}\sum_{i}^{N}\nabla_i^2}^{T} + \overbrace{\sum_{i=1}^{N}\sum_{j>i}^{N}\frac{1}{|\boldsymbol{r}_i-\boldsymbol{r}_j|}}^{V_{\text{int}}} \overbrace{-\sum_{i=1}^{N}\sum_{I=1}^{M}\frac{Z_i}{|\boldsymbol{r}_i-\boldsymbol{R}_I|}}^{V_{\text{ext}}} \underbrace{-\frac{1}{2}\sum_{I=1}^{M}\frac{\nabla_I^2}{M_I}}_{T_{\text{ion}}} + \underbrace{\sum_{I=1}^{M}\sum_{\mathcal{J}>I}^{M}\frac{Z_I Z_{\mathcal{J}}}{|\boldsymbol{R}_I-\boldsymbol{R}_{\mathcal{J}}|}}_{E_{\text{nn}}} \tag{5.3}$$

where $M_I, Z_I, \boldsymbol{R}_I$ denote the mass, charge and position of the nuclei, respectively, and $\boldsymbol{r}_i$ are the positions of the electrons. Exact solutions to Eq. (5.2) are only possible for 1-body systems or 2-body systems that can be reduced into 1-body problems, as is the case of an isolated hydrogen atom. In all other cases, one must resort to approximations and numerical solutions. If the approximations giving rise to a certain method are of such nature that the resulting equations are free from adjustable physical parameters, the method is customarily referred to as an *ab initio* or *first-principles* method.

5.1.1 The Born-Oppenheimer approximation

A common approximation for many methods seeking to solve Eq. (5.2) for the Hamilton operator in Eq. (5.3) is to make use of the fact that the nuclei are much heavier than the electrons. For the electrons this means that they see the nuclei as charges frozen in their instantaneous location, hence the nuclear kinetic energy term can be dropped and the ion-ion repulsion V_{nn} simply amounts to a constant shift of the Hamilton operator. This is known as the *Born-Oppenheimer approximation* [84] and allows us to write a simplified electronic Hamilton operator

$$H_{\text{e}} = T + V_{\text{int}} + V_{\text{ext}}. \tag{5.4}$$

With the spin variables suppressed, the time-independent Schrödinger equation for the electrons now reads

$$H_e\Psi_e(\{\boldsymbol{r}_i\};\{\boldsymbol{R}_I\}) = E_e\Psi_e(\{\boldsymbol{r}_i\};\{\boldsymbol{R}_I\}) \tag{5.5}$$

and the total energy is $E_{\text{tot}} = E_e + E_{nn}$. Similarly, one can write a separate Schrödinger equation for the nuclei, which can then be regarded as moving in a mean-field generated by the electrons. Here, a full quantum mechanical treatment is often not necessary and the nuclei can be regarded as classical particles moving in the potential $E_{\text{tot}}(\{\boldsymbol{R}_I\})$ obtained by solving the electronic problem Eq. (5.5) and often referred to as the *potential energy surface*. The force on a nuclei I is given by

$$\boldsymbol{F}_I = -\frac{\partial}{\partial \boldsymbol{R}_I} E_{\text{tot}}(\{\boldsymbol{R}_I\}) = -\left\langle \Psi \left| \frac{\partial H}{\partial \boldsymbol{R}_I} \right| \Psi \right\rangle - \underbrace{E \frac{\partial}{\partial \boldsymbol{R}_I} \langle \Psi | \Psi \rangle}_{=0 \text{ if basis is complete}} . \tag{5.6}$$

This is known as the *Hellmann-Feynman* theorem and evaluation of the first term in Eq. (5.6) shows that the forces on the ions are simply the electrostatic forces due to the electronic charge distribution. Numerical solutions to the Schrödinger equation are typically based on a basis expansion of the wavefunction (Sect. 5.2.5), however, and only a finite number of such functions can be included. In this case, the derivative in the second term in Eq. (5.6) is not zero if the basis functions depend on the ionic positions. As a result the ions experience so-called *Pulay forces* that need to be corrected for according to Eq. (5.6).

Despite greatly simplifying the original problem, Eq. (5.4) further theoretical development is required to obtain equations can be solved, at least numerically.

5.2 Density functional theory

Density functional theory (DFT) is one of the cornerstones of modern computational materials physics and provides a way of solving the Schrödinger equation to a high degree of accuracy with an efficiency that makes calculations involving several hundreds of atoms tractable on modern supercomputers. As alluded to by the name, the electronic density plays a fundamental role in this theory and is defined in terms of the many-body electronic wavefunction from Eq. (5.4) as

$$n(\boldsymbol{r}) = \int d\boldsymbol{r}_2 \dots d\boldsymbol{r}_N \left|\Psi(\boldsymbol{r}, \boldsymbol{r}_2, \dots, \boldsymbol{r}_N)\right|^2 \tag{5.7}$$

where the subscript has been dropped from Ψ_e and the parametric dependence on the nuclear coordinates has been suppressed.

5.2.1 The Hohenberg-Kohn theorems

The theoretical foundation of DFT rests on the shoulders of two theorems proved by Hohenberg and Kohn (HK) in 1964 [85]. We shall be content with giving a concise summary of them here, for a more detailed account readers are referred to one the many textbooks covering the topic [86, 87]. For a stationary, interacting, non-degenerate system of electrons there is a one-to-one mapping between V_{ext}, $|\Psi_0\rangle$ and $n(\boldsymbol{r})$. Consequently, the ground state is a *functional* of the ground state density, which is denoted $|\Psi[n]\rangle$. This functional is unique and takes the same form regardless of V_{ext} if V_{int} does not change. This implies in turn that the ground state expectation value of any observable is also a functional of the density

$$O[n] = \langle \Psi[n] | \, O \, | \Psi[n] \rangle \, . \tag{5.8}$$

Of particular interest is the ground state energy

$$E[n] = \langle \Psi[n] | \, H_e \, | \Psi[n] \rangle = \langle \Psi[n] | \, T + V_{\text{int}} \, | \Psi[n] \rangle + E_{\text{ext}} \tag{5.9}$$

where the the external energy functional

$$E_{\text{ext}}[n] = \int d\boldsymbol{r} \, n(\boldsymbol{r}) V_{\text{ext}}(\boldsymbol{r}). \tag{5.10}$$

has been defined. The total energy functional in Eq. (5.9) can be shown to obey a variational principle with a minimum corresponding to the true ground state density, i.e.

$$E[n] < E[n'] \, , \forall n' \neq n \tag{5.11}$$

An appealing feature of these results is that the unwieldy many-body wavefunction in bypassed favor of the electronic ground state density, a scalar function of only three variables. Note however, that the HK theorems are pure existence theorems and do not contain a recipe for constructing an explicit expression for $E[n]$ that would allow for determination the ground-state energy and other observables.

5.2.2 Kohn-Sham theory

Kohn-Sham (KS) theory provides us with a way of leveraging the Hohenberg-Kohn theorems to derive a practical scheme for determining the ground state density of a system [88]. It rests on the non-trivial assumption that a system of interacting electrons can be mapped onto a system of fictitious, non-interacting electrons in such a way that the ground-state electron density is the same for the two systems. This new system is typically referred to as the KS auxiliary system and its existence has not been proved for the general case; rather it is typically justified from a practical perspective by the remarkable success of KS theory in predicting many material properties. Since the KS system is non-interacting, it can be described by a set of single-particle, Schrödinger-like equations

$$\underbrace{\left[-\frac{1}{2} \nabla^2 + V_{\text{KS}}(\boldsymbol{r}) \right]}_{\equiv H_{\text{KS}}} \Psi_i(\boldsymbol{r}) = \epsilon_i \Psi_i(\boldsymbol{r}). \tag{5.12}$$

The density is then simply $n(\boldsymbol{r}) = \sum_i f_i |\Psi_i(\boldsymbol{r})|^2$, where f_i is the occupation number of orbital i. Here, V_{KS} is an effective potential for which a useful expression can be derived by decomposing the energy functional for the KS system according to

$$E_{\mathrm{KS}} = T_s[n] + E_{\mathrm{H}}[n] + E_{\mathrm{xc}}[n] + E_{\mathrm{ext}}[n] \tag{5.13}$$

where the very first term is the kinetic energy functional

$$T_s[n] = -\frac{1}{2}\sum_i f_i \Psi_i(\boldsymbol{r})\nabla^2\Psi_i(\boldsymbol{r}). \tag{5.14}$$

The interactions of the original many-body problem, other than those coming from the external potential, are reflected by the interacting KS density in the other two terms E_H and E_{xc}. The first of these terms is the Hartree energy functional

$$E_H[n] = \frac{1}{2}\int d\boldsymbol{r}\, d\boldsymbol{r}'\, \frac{n(\boldsymbol{r})n(\boldsymbol{r}')}{|\boldsymbol{r}-\boldsymbol{r}'|}. \tag{5.15}$$

The last term E_{xc} in Eq. (5.13) is known as the *exchange-correlation* functional and is defined to contain all many-body effects such that the ground state density of the KS system will indeed be equal to that of the original interacting system. By using the Hohenberg-Kohn variational principle for E_{KS}, a set of independent electron equations of the form Eq. (5.12) is obtained with

$$V_{\mathrm{KS}} = \underbrace{\int d\boldsymbol{r}'\, \frac{n(\boldsymbol{r}')}{|\boldsymbol{r}-\boldsymbol{r}'|}}_{\equiv V_H(\boldsymbol{r})} + \underbrace{\frac{\delta E_{\mathrm{xc}}}{\delta n(\boldsymbol{r})}}_{\equiv V_{\mathrm{xc}}(\boldsymbol{r})} + V_{\mathrm{ext}}(\boldsymbol{r}). \tag{5.16}$$

Once the KS equations in (5.12) have been solved the ground state energy can be calculated as

$$E_0 = \sum_i f_i\epsilon_i - E_H[n(\boldsymbol{r})] - \int d\boldsymbol{r}\, n(\boldsymbol{r})V_{\mathrm{xc}}(\boldsymbol{r}) + E_{\mathrm{xc}}[n]. \tag{5.17}$$

5.2.3 Approximating the exchange-correlation functional

The ground state energy as calculated from the KS system as in Eq. (5.17) is exact provided that exact expressions for all terms in Eq. (5.16) are known. This is, however, not the case for the exchange-correlation functional E_{xc}, which was defined to capture all the many-body effects not included by the other terms. E_{xc} constitutes the major source of approximation in DFT.

Short of neglecting E_{xc} altogether, the simplest approach one can take is the *local density approximation* (LDA), in which a differential volume $d\boldsymbol{r}$ is assumed to give a contribution to the total exchange-correlation energy equal to the energy density of a homogeneous electron gas (HEG) having density $n(\boldsymbol{r})$ so that

$$E_{\mathrm{xc}}^{\mathrm{LDA}} = \int d\boldsymbol{r}\, n(\boldsymbol{r}) \epsilon_{\mathrm{xc}}^{\mathrm{LDA}}[n(\boldsymbol{r})], \tag{5.18}$$

where $\epsilon_{\mathrm{xc}}^{\mathrm{LDA}}$ is the HEG energy density. Note that this expression is purely *local* in the sense that $E_{\mathrm{xc}}^{\mathrm{LDA}}$ is the sum of point-wise evaluated contributions. A natural extension is to consider also variations in the density i.e., make use of the gradient $|\nabla n(\boldsymbol{r})|$ and possibly higher order derivatives, referred to as a *generalized-gradient approximation* (GGA)

$$E_{\mathrm{xc}}^{\mathrm{GGA}} = \int d\boldsymbol{r}\, n(\boldsymbol{r}) \epsilon_{\mathrm{xc}}^{\mathrm{GGA}}[n(\boldsymbol{r}), |\nabla n(\boldsymbol{r})|, |\nabla^2 n(\boldsymbol{r})|, \ldots]. \tag{5.19}$$

Such approximations are termed *semi-local* to indicate that the contributions, while still evaluated at a point, take the infinitesimal environment into account through the inclusion of density derivatives. A popular GGA-type method is the Perdew-Burke-Ernzerhof (PBE) functional [89], which takes into account first-order variations of the density.

5.2.4 Dispersion-corrections

A major shortcoming of local or semi-local exchange-correlation functional is that they do not account for dispersive interactions. These interactions are inherently non-local and thus connect the electron density at different points in space. Therefore, from the functional forms Eqs. (5.18) and (5.19) of LDA and GGA-type functionals it is apparent that they by definition cannot include non-local effects.

A simple and efficient approach to include dispersive interactions is the DFT-D method [90], which in its most basic form introduces an interatomic pair potential with the correct asymptotic $1/r^6$-form to the total DFT energy E_0 in Eq. (5.17),

$$E_0^{\text{DFT-D}} = E_0 + \sum_{Ij} \frac{C_6^{Ij}}{R_{Ij}^6}. \tag{5.20}$$

The C_6-coefficients appearing in this equation are fitted to dispersive interactions between molecules calculated using quantum-chemistry methods. There are many drawbacks to this method [91]: the C_6-coefficients are agnostic to the local environment, there is no screening, only the first order correction to the vdW energy is taken into account (see Appendix A), and the correct short-range vdW behavior is not reproduced. While the two latter deficiencies are addressed to some extent in later incarnations of the method [92, 93], it is still fundamentally semi-empirical in nature since it relies on the availability of accurate values for the C_6-coefficients. For many systems, in particular molecular ones, this level of treatment may prove sufficient, but since vdW

interaction are typically weak even small inaccuracies can yield results that are qualitatively wrong. Several other dispersion-correction methods are available that suffer these drawbacks to varying degrees [94, 95, 96].
An ab initio approach to the problem is provided by the van der Waals density functional (vdW-DF) framework. The underlying theory has a long history and is quite involved, hence only a brief overview is given here and the curious reader is referred to more detailed accounts [97, 98]. The vdW-DF framework has given birth to a family of functionals that can be written in the general form

$$E_{\mathrm{xc}}^{\text{vdW-DF}}[n] = E_{\mathrm{x}}^{\mathrm{GGA}}[n] + E_{c}^{\mathrm{LDA}}[n] + E_{\mathrm{c}}^{\mathrm{nl}}[n]. \tag{5.21}$$

Each family member is thus the sum of the exchange part of a suitably chosen GGA companion functional, local LDA correlation and a non-local correlation functional. The latter functional can be written

$$E_{\mathrm{nl}}[n] = \frac{1}{2}\int d\boldsymbol{r}\, d\boldsymbol{r}'\; n(\boldsymbol{r})K(\boldsymbol{r},\boldsymbol{r}')n(\boldsymbol{r}') \tag{5.22}$$

and accounts for the dispersive interactions. Here, the integration kernel $K(\boldsymbol{r},\boldsymbol{r}')$ contains information about how strongly two density regions interact depending on their spatial separation and the asymmetry of their response. While approximations are made in deriving Eqs. (5.21) and (5.22), no adjustable parameters with physical significance, akin to the C_6 coefficients of the DFT-D method, are introduced and hence vdW-DF constitutes a genuine first-principles method. It should also be clarified that while the larger vdW-DF framework accounts for many-body dispersion effects, approximations made in deriving the actual functional Eq. (5.22) limit the inclusion of such effects to length scales corresponding to typical binding distances. This is easily overlooked since Eq. (5.22) has the form of a double summation and the information about screening is effectively hidden in the kernel [98].

A practical problem encountered when implementing a vdW-DF functional is that straightforward numerical evaluation of the six-dimensional integral Eq. (5.22) is much too costly. To bring the computational effort required to a manageable level, a method due to Román-Pérez and Soler can be employed where the kernel is effectively tabulated in terms of two parameters. The non-nocal energy can subsequently be calculated by fast Fourier transforms and three-dimensional integrations [99]. This is the subject of **Paper II**, which describes a reference implementation in the form of a `C`-library that make vdW-DF functionals available to an interfacing DFT code.

Two of most most prolific vdW-DF family members are vdW-DF1 [100]

$$E_{\mathrm{xc}}^{\text{vdW-DF1}}[n] = E_{\mathrm{x}}^{\mathrm{revPBE}}[n] + E_{c}^{\mathrm{LDA}}[n] + E_{\mathrm{c}}^{\mathrm{nl}(1)}[n], \tag{5.23}$$

and vdW-DF2 [101]

$$E_{\mathrm{xc}}^{\text{vdW-DF2}}[n] = E_{\mathrm{x}}^{\text{PW86r}}[n] + E_{c}^{\text{LDA}}[n] + E_{\mathrm{c}}^{\text{nl}(2)}[n]. \tag{5.24}$$

Note that the non-local correlation functionals used above differ slightly with regards to an underlying approximation and are consequently accompanied by different exchange functionals. For vdW-DF1 the conventional choice is the revised version of PBE by Zhang-Yang (revPBE) [102] and for vdW-DF2 it is the refitted Perdew-Wang functional (PW86r) [103]. A more recent addition to the family is vdW-DF-cx [104]

$$E_{\mathrm{xc}}^{\text{vdW-DF-cx}}[n] = E_{\mathrm{x}}^{\text{LV-PW86r}}[n] + E_{c}^{\text{LDA}}[n] + E_{\mathrm{c}}^{\text{nl}(1)}[n]. \tag{5.25}$$

The new feature is an exchange companion termed LV (Langreth-Vosko)-PW86r that utilizes concepts from the vdW-DF framework also for the description of the exchange contribution. In **Paper I**, the use of vdW-DF-cx was crucial in obtaining accurate results for inter-chain and surface-chain vdW interactions of thiols on gold, while maintaining a good description of the surface. Indeed, it has been demonstrated that vdW-DF-cx yields excellent agreement with experimental values for many bulk properties of a large set of solids [105].

5.2.5 Solving the Kohn-Sham equations

Given a suitable approximation for the exchange-correlation functional the KS equations (5.12) remain to be solved, a formidable challenge in itself. From Eqs. (5.12) and (5.16) it is seen that V_{KS}, which naturally must be known in order for the KS equations to be completely specified, depends on the density, which in turn cannot be known before the KS equations have been solved. To progress from this circular situation, a *self-consistent* approach must be taken in solving the equations. This means that a reasonable starting density is constructed, usually from atomic orbitals, and used to determine V_{KS} so that the KS equations may be solved. The states $|\Psi_i\rangle$ thus obtained are then combined into a new density and the whole process is repeated iteratively until convergence, according to some judiciously chosen criterion, is achieved.

To actually solve the KS set of single-particle equations Eq. (5.12), a common approach is to expand the orbitals in terms of a basis $\mathscr{B}$ for the Hilbert space

$$|\Psi\rangle = \sum_{b} \langle b|\Psi\rangle \, |b\rangle \,, \tag{5.26}$$

where the sum extends over all $b \in \mathscr{B}$ and the orbital index i has been dropped for convenience. Substituting this expressions into Eq. (5.12) and multiplying from the left with $|b'\rangle$ yields

$$\sum_{b} \langle b' \left| H_{\mathrm{KS}} \right| b\rangle \, \langle b|\Psi\rangle = \epsilon \sum_{b} \langle b'|b\rangle \, \langle b|\Psi\rangle \,, \tag{5.27}$$

which has the form of a generalized matrix eigenvalue problem

$$\boldsymbol{H}_{\mathrm{KS}}\boldsymbol{\Psi} = \epsilon \boldsymbol{S}\boldsymbol{\Psi}, \tag{5.28}$$

where

$$\begin{aligned} \boldsymbol{H}_{\mathrm{KS}} &= \left[\langle b' \,\middle|\, H_{\mathrm{KS}} \,\middle|\, b\rangle\right]_{b,b'\in\mathscr{B}} \\ \boldsymbol{\Psi} &= \left[\langle b|\Psi\rangle\right]_{b\in\mathscr{B}} \\ \boldsymbol{S} &= \left[\langle b' \,\middle|\, b\rangle\right]_{b,b'\in\mathscr{B}} \end{aligned} .$$

By only including a finite number of elements in the basis expansion (5.26) the problem can be solved numerically and if the basis set is furthermore orthogonal, the overlap matrix $\boldsymbol{S}$ reduces to the identity matrix and an ordinary eigenvalue problem is obtained. What basis set to choose depends on the problem at hand, since even if any orthonormal set can in principle be used, the resulting computational effort can vary significantly.

5.2.6 Periodic systems and plane waves

For a system with periodic boundary conditions, such as a crystal, the wavefunction can be expanded in terms of plane waves and Bloch's theorem asserts that for energy eigenfunctions this expansion takes the form [106]

$$|\Psi_{\boldsymbol{k}}\rangle = \sum_{\boldsymbol{G}} c_{\boldsymbol{k}+\boldsymbol{G}} \,|\boldsymbol{k}+\boldsymbol{G}\rangle\,, \tag{5.29}$$

where $\boldsymbol{G}$ is a reciprocal lattice vector and $|\boldsymbol{k}\rangle$ represents a plane wave state, i.e. $\langle \boldsymbol{r}|\boldsymbol{k}\rangle \sim e^{i\boldsymbol{k}\cdot\boldsymbol{r}}$. The wave vector $\boldsymbol{k}$ is continuous and arbitrary but can be restricted to lie in the first Brillouin zone. Note that for molecules and other systems with no inherent periodicity, it can be artificially introduced by periodically inserting mirror images of the system with enough separation that any interaction between them effectively vanishes.

Using the notation for the matrix elements introduced in the previous section, the overlap matrix $\boldsymbol{S}$ is equal to the unit matrix since plane waves are orthogonal. Furthermore, given the Fourier expansion for the periodic potential

$$V_{\mathrm{KS}}(\boldsymbol{r}) = \sum_{\boldsymbol{G}} v_{\boldsymbol{G}} e^{i\boldsymbol{G}\cdot\boldsymbol{r}}, \tag{5.30}$$

the matrix elements of the KS Hamilton operator can be written

$$\langle \boldsymbol{k}+\boldsymbol{G}' \,|\, H_{\mathrm{KS}} \,|\, \boldsymbol{k}+\boldsymbol{G}\rangle = \frac{1}{2}\,|\boldsymbol{k}+\boldsymbol{G}|^2\,\delta_{\boldsymbol{G}\boldsymbol{G}'} + v_{\boldsymbol{G}-\boldsymbol{G}'}\,. \tag{5.31}$$

The expansion is truncated by choosing a kinetic energy cutoff for the plane waves according to $|\boldsymbol{k}+\boldsymbol{G}| = \sqrt{2E_{\mathrm{cut}}}$, thus providing a simple, systematic way of improving the

accuracy in a DFT calculation. Other advantages of plane wave expansions include the absence of Pulay forces[1], numerical efficiency due to the use of fast Fourier transforms, and the orthogonality of the basis.

The major issue with plane wave expansions lies in the description of the atomic core region, where the kinetic energy of the electrons is high and the wave function varies rapidly. This implies that, due to their delocalized nature, an extremely high number of plane waves would be required to accurately represent the electronic density in this region. The situation can be remedied by introducing a so-called *pseudopotential* [87], which makes use of the fact that it is typically only the valence electrons, and not the core electrons, that participate in the chemical bonding. Accordingly, the pseudopotential is modified to achieve smoother variations of the wavefunction within the core region while still reproducing the correct all-electron wave function outside. This results in a dramatic decrease in the plane wave cutoff E_{cut} required for convergence and makes plane wave expansions feasible for practical calculations. The trade-off is one of introducing additional complexity; pseudopotentials need to be explicitly constructed for all atomic species involved and the size of the core region needs to be chosen appropriately. Pseudopotentials come in one of two different flavors: *norm-conserving* or *ultrasoft*, where the latter require lower cutoff energies. Ultrasoft pseudopotential have furthermore been shown to emerge naturally from the more rigorous framework of *projector augmented waves* (PAW) [107, 108]. Here, a linear transformation for converting between a valence and all-electron description is defined and different levels of treatment with regards to the core electrons are possible. For most practical purposes the initial core electron configuration for which the PAW potential was generated is kept throughout the calculation in what is called the *frozen core* approximation [109].

Another problem that emerges in periodic DFT calculations is that many properties, such as the total energy of the system, are given in terms of integrals over the first Brillouin zone (BZ) of the system

$$I = \frac{\Omega}{(2\pi)^3} \sum_{n}^{\text{occ}} \int_{\text{BZ}} d\boldsymbol{k}\, I_n(\boldsymbol{k}), \tag{5.32}$$

where I denotes some property, Ω the unit cell volume and the summation runs over all occupied bands. To numerically evaluate the $\boldsymbol{k}$-space integral, it is replaced by a summation over a finite amount of $\boldsymbol{k}$-points sampled from the Brillouin zone. A common sampling method is the Monkhorst-Pack scheme [110] where $M_1 \times M_2 \times M_3$ $\boldsymbol{k}$-points lie on an equidistant grid aligned with the reciprocal lattice vectors $\boldsymbol{b}_i$ according to the rule

[1] This is only true as long as the cell metric does not change and thus Pulay forces and stresses have to be corrected for during unit cell relaxations.

$$\boldsymbol{k} = x_1 \boldsymbol{b}_1 + x_2 \boldsymbol{b}_2 + x_3 \boldsymbol{b}_3 \quad \text{with} \quad x_i = \frac{2m_i - M_i - 1}{2M_i},\ m_i \in \left\{1, 2, \ldots, M_i\right\}. \tag{5.33}$$

Furthermore, by properly weighting the terms in the summation approximating the integral Eq. (5.32), only those BZ $\boldsymbol{k}$-points that are inequivalent under the symmetries of the space group need to be included[2].

[2]The set of all such point is referred to as the irreducible Brillouin zone.

6

Summary of appended papers

6.1 Paper I

This paper originated as a means of gauging the accuracy of vdW-DF-cx (Sect. 5.2.4) in the description of systems, in which a molecule with a long alkyl chain chemisorbs on a noble metal surface, as ultimately required for DFT studies of CTAB on gold. In this context, earlier functionals in the vdW-DF family such as vdW-DF1 were frequently overlooked due to gross overestimations of lattice constants, especially for the late transition metals Ag and Au.

Rather than directly performing the calculations of CTAB on gold with vdW-DF-cx, it was advantageous to first study a system with more experimental and theoretical data available as reference points. Here, alkanethiolates on Au{111} proved an ideal candidate system: it functions as a prototype for a wider class of self-assembly systems, is in itself relevant for many applications, and has been extensively studied in the recent decades. The idea was to study the role of dispersive interaction in transitions between the experimentally observed low coverage lying-down phases and more dense standing up phases of the system using an ab initio thermodynamics model (Sect. 3.1).

The vdW-DF-cx metho was found to provide an excellent description, not only for the dispersive interaction but also for the gold surface. Indeed, CX offers significant improvement over the PBE values for both the lattice constant and clean surface energy. Furthermore, lying-down phases, characterized by chemisorbed thiolates that lie almost parallel to the surface were revealed to be thermodynamically stable for alkyl chains with two or more methylene units. With increasing gas-phase chemical potential a transition to a standing-up phase was observed. The most significant finding was that these transitions emerge due to a competition between alkyl chain-chain and chain-surface interactions. More precisely, the chain-surface interactions vary more

steeply with the chain length, and the interaction strength was shown to be in very good agreement with experimental data.

6.2 Paper II

This paper concerns the implementation of `libvdwxc`, a `C`-library with the aim of providing DFT codes with easy and efficient access to all vdW-DF family functionals. More precisely, the library computes the non-local vdW-DF correlation energy (Eq. (5.22)) given the density and its gradient as input from the interfacing DFT code. To obtain a specific vdW-DF functional, the non-local correlation energy thus obtained must be combined with the exchange part of the corresponding companion GGA functional and LDA correlation.

Due to the six-dimensional nature of the non-local correlation integral (Eq. (5.22)), direct integration is not viable. Instead, `libvdwxc` employs the method of Román-Pérez and Soler [99]. Briefly, the kernel is represented in terms of radial functions on a two-dimensional grid and spline-based interpolations are used to obtain high accuracy. The non-local correlation can then be computed using the convolution theorem, which reduces the six-dimensional integration to a summation over three-dimensional integrals. Several Fourier transforms must be calculated during this process, which limits the overall scaling of the method to $\mathcal{O}(n \log n)$ where n is the number of real-space grid points used.

The accuracy of the library is benchmarked over the S22 set of dimers[1] and good agreement with corresponding implementations in `VASP` and `Quantum Espresso` is obtained. Furthermore, parallelization is available through MPI; the scaling of parallel calculations with respect to the number of cores is measured for a ligand-protected gold nanoparticle consisting of 2424 atoms. It is found that the evaluation the non-local correlation energy is generally efficient enough to not impose any additional limitations on system size compared to DFT calculations with conventional semi-local functionals.

[1] The data set consists of 22 dimers that generally exhibit dispersion and/or hydrogen bonding, with reference energies accurate quantum chemical calculations.

7 Outlook

In the fields of observation chance favors only the prepared mind.

Louis Pasteur

In the pursuit of a mechanistic understanding of gold nanorod growth, the results and discussion in Chapter 4 provide plenty of direction for future work. An estimated timeline for upcoming publications[1] is shown in Fig. 7.1.

I *Plasmonic sensing of surfactant structure* As the immediate next step on the research track, the surface phase diagram of CTAB on silica will be established by a combination of MD simulations and experiment. While from an applications point of view this is a relevant system in itself, it will also serve as a means of gauging the predictive power of the MD simulations. In this work, my role will be to contribute to the analysis of the MD simulations and experimental data and participate in writing the paper.

II *Phase transitions in surfactant structure guide nanoparticle growth.* Supported by the results of the paper outlined above, the central theme of this publication is the surface phase diagram of CTAB on gold. A similar combination of simulations and experiment will be used, where the former to a large extent consists of the material found in Sect. 4.2. The phase diagram will be analyzed and put into the context of the channel model of gold nanorod growth. Here, I will write the bulk of the paper, help direct the MD simulations/experiments and contribute to the analys thereof.

[1] The titles of all unpublished work should be considered as tentative. Furthermore, only planned publications for which data has already been gathered are shown.

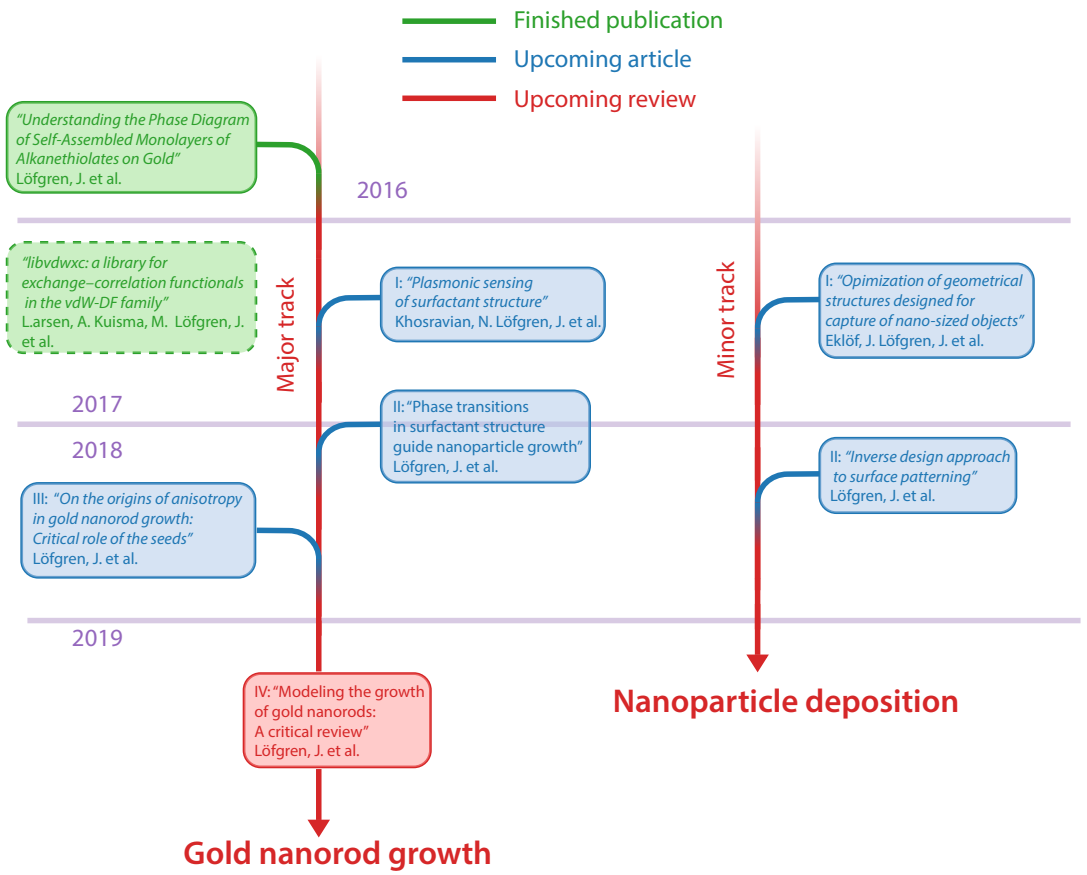

Figure 7.1: An estimated timeline and plan for future publications. There are two distinct research tracks: gold nanorod growth (major) and nanoparticle deposition (minor).

III *On the origins of anisotropy in gold nanorod growth: the critical role of the seed.* This paper will primarily expand on the ideas developed in Sect. 4.3, namely the role of the structure of the seeds in gold nanorod growth. Of particular interest is the difference between seeds in the **P-1** and **P-2** protocols, respectively. DFT calculations will be used as input to an ab initio thermodynamics model (Sect. 3.1). Once surface free energies have been obtained as functions of the chemical environment, they will be used to predict nanoparticle shapes using Wulff constructions (Sect. 3.2). Since the inclusion of twinned structures is crucial in this context, the standard Wulff construction is not sufficient and an extension of the technique will be required. My role here will be to perform the bulk of the calculations, possibly with some assistance in constructing extended Wulff shapes, and write the paper. Surface diffusion of gold atoms on low-index facets may also be included in the

investigations.

IV *Modeling the growth of gold nanorods: a critical review.* Pending the outcome of the investigations outlined above, a comprehensive review will published towards the end of my doctoral studies. The purpose will be to provide a broad survey of modeling approaches to nanorod growth taken in literature, as well as to summarize our own findings. The majority of this review would be written by myself, with smaller contributions from several coworkers.

As indicated in Fig. 7.1, another research track is being pursued concurrently. The overarching topic is the modeling of nanoparticle deposition problems. A detailed description of these invesgations, which are already underway, was considered to be out of the scope of this thesis. Nevertheless, brief descriptions of two upcoming publications are included below for completeness.

I *Optimization of geometrical structures designed for capture of nano-sized objects.* This publication represents a joint effort between experimental work carried out in the Molecular Materials group at Chalmers and theoretical modeling. The goal is the optimization of gold nanoparticle deposition onto lithographically pre-patterned metal or semi-conductor substrates. The starting point for the modeling effort is the extension of so-called random sequential adsorption (RSA) models, which rely on analytical inter-particle potentials derived from elementary DLVO theory (Sect. 2.5.2). In deriving such potentials, assumptions concerning the interacting particles geometry have to be made that limit their usefulness for the problem at hand. Therefore, a crucial part of the work concerns general-geometry extensions of interactions models for colloidal nanoparticles. Here, my role is to develop the required methodology, implement the resulting algorithm, analyze the results and write the modeling part of the paper.

II *Inverse design approach to surface patterning.* Using the extended RSA and DLVO framework developed in the previous publication in conjunction with statistical optimization methods, e.g., genetic algorithms, an inverse design approach to surface patterning will be constructed. The outcome will be a model that takes as input a cost function encoding the goal of the optimization, e.g., to deposit particles in a given configuration, and yields as output a corresponding optimized patterning for the surface. Here, I would be responsible for constructing and implementing the model and write the paper.

A Origin of the dispersive interaction

Each half of the cosmic breath, moved by a void.

Vektor, *Terminal Redux: Recharging the Void*

The origin of dispersive interactions and their asymptotic $1/R^6$-dependence can be demonstrated from elementary quantum mechanics, without appealing to classical concepts or a model system, by considering the interaction between two well-separated hydrogen atoms. A coordinate system according to Fig. A.1 is defined, where the nuclei a, b have a relative displacement $\boldsymbol{R}$ and the electrons are displaced from their respective parent nucleus by $\boldsymbol{r}_1$ and $\boldsymbol{r}_2$. The full non-relativistic, electronic Hamiltonian can be expressed as the sum of the Hamiltonians of each isolated atom plus an interaction term

$$H = \underbrace{-\frac{1}{2}\boldsymbol{p}_1^2 - \frac{1}{r_1}}_{\equiv H_a} \underbrace{-\frac{1}{2}\boldsymbol{p}_2^2 - \frac{1}{r_2}}_{\equiv H_b} + \underbrace{\left(\frac{1}{R} + \frac{1}{r_{12}} - \frac{1}{r_{1b}} - \frac{1}{r_{2a}}\right)}_{\equiv V}. \tag{A.1}$$

The idea is now to treat V as a perturbation on the Hamiltonian $H_0 = H_a + H_b$. Using the familiar labels (n, l, m) for the hydrogen atom quantum numbers, the energy eigenstates of the unperturbed Hamiltonian have the form

$$|p^{(0)}\rangle = |nlm\rangle_a \otimes |n'l'm'\rangle_b \equiv |nlm\rangle\,|n'l'm'\rangle\,, \tag{A.2}$$

where $p = (n, l, m, n', l', m')$ is a compound index and the (0) superscript indicates that the kets are only exact eigenstates for H_0 and not the full interacting Hamiltonian. The corresponding eigenvalues are

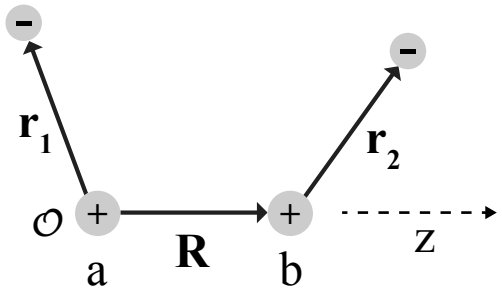

Figure A.1: Coordinate system used in the derivation of the dispersive interaction between two hydrogen atoms. The origin is taken to coincide with nucleus a and the z-axis is parallel to the relative displacement vector of the nuclei. Note that the displacement vector for the second electron is given relative to the parent nucleus rather than the origin.

$$\left\langle p^{(0)} \middle| H_0 \middle| p^{(0)} \right\rangle = \langle nlm \middle| H_a \middle| nlm \rangle + \langle n'l'm' \middle| H_b \middle| n'l'm' \rangle \equiv E^{(0)}_{n,n'} \tag{A.3}$$

and in particular the ground state energy is given by $E^{(0)}_{11} = -1\,\mathrm{Ha}$[1]. The next step is to write a multipole expansion of the perturbing potential by summing Taylor expansions of the individual terms in V. For the interaction of the first nuclei and the second electron:

$$\frac{1}{r_{2a}} = \frac{1}{\left|\boldsymbol{R} + \boldsymbol{r}_2\right|} = \frac{1}{R} + \frac{\boldsymbol{R}\cdot\boldsymbol{r}_2}{R^3} + \text{higher order terms.} \tag{A.4}$$

The other terms have similar expansions and upon summation of the results it is apparent that the monopole terms cancel as expected for neutral atoms. Furthermore, assuming that the atoms are well separated, i.e., $R >> a_0$ where a_0 is the Bohr radius, only the dipole term in Eq. (A.4) needs to be retained. The final expression is, after some algebra,

$$V \approx \frac{1}{R^3}\left(x_1x_2 + y_1y_2 - 2z_1z_2\right). \tag{A.5}$$

The first order perturbation of the ground state energy is now evaluated as

$$W_1 = \frac{1}{R^3}\langle 100 \middle| x_1x_2 + y_1y_2 - 2z_1z_2 \middle| 100\rangle = 0 \tag{A.6}$$

due to parity since $|100\rangle$ is even and V is odd. The second order perturbation cannot be exactly evaluated but is given by the series

[1] 1 Hartree (Ha) is equal to 2 Ry = 27.21138602(17) eV

$$W_2 = \sum_{n',n\neq 1} \sum_{\substack{l',m' \\ l,m}} \frac{\left|\langle 100|\,\langle 100\,|\,V\,|\,nlm\rangle\,|n'\,l'\,m'\rangle\right|^2}{E_{11}^{(0)} - E_{nn'}^{(0)}}, \tag{A.7}$$

where it is apparent that each term is negative and scales like $1/R^6$. It follows that to leading order the ground state energy of two well-separated neutral atoms can be written

$$E_0 = E_{11}^{(0)} + W_2 = -1 - \frac{C_6}{R^6}, \tag{A.8}$$

where C_6 is an unknown coefficient that needs to be calculated numerically. In conclusion, the correction W_2 describes a dipole-dipole type interaction, stemming from the electrostatic coupling the atoms experience in each others proximity. This is customarily referred to as the van der Waals interaction and results in a negative shift of the ground state energy. Since neither atom has a net dipole moment, the van der Walls interaction can be thought of as an induced dipole-induced dipole interaction as typically presented in literature. This simplified picture can, however, be misleading since it gives an impression that the phenomenon is time-dependent, when the above derivation shows that this is clearly not the case.

Acknowledgments

I wish to extend my most sincere thanks to my supervisor Paul Erhart for educating me in physics, references to popular culture, and so many other things. Above all else, however, I would like to thank you for teaching me the value of being perpetually curious. I am also grateful to my examiner Göran Wahnström for his wisdom, guidance and in particular for creating an open, inquisitive, and friendly working environment. It would of course not be much of a working environment without a set of wonderful colleagues; thank you all for your friendship, good conversation, and evenings at Foxes.

One of the greatest joys of working in a university is the proximity to virtually endless sources of inspiration and different perspectives. In this spirit I would like to thank my co-supervisor Kasper Moth-Poulsen and the rest of the Molecular Materials group for helping me broaden my horizons and being all around great people. The same goes for all my collaborators, past and present: Mikael Kuisma, Babak Sadigh, Johnas Eklöf, Ask Hjorth Larsen, Henrik Grönbeck, Per Hyldgaard and many others.

Last but not least, I extend my love and thanks to my family and close friends in Göteborg and all around the world. You brighten my days and keep me sane amidst all the equations.

Until next time,

Joakim

Bibliography

[1] L. B. Hunt, *The true story of Purple of Cassius*, Gold Bulletin **9**, 134 (1976).

[2] D. Akinwande, N. Petrone, and J. Hone, *Two-dimensional flexible nanoelectronics*, Nature Communications **5**, 6678 (2014).

[3] S. K. Murthy, *Nanoparticles in modern medicine: State of the art and future challenges*, International Journal of Nanomedicine **2**, 129 (2007).

[4] E. Serrano, G. Rus, and J. García-Martínez, *Nanotechnology for sustainable energy*, Renewable and Sustainable Energy Reviews **13**, 2373 (2009).

[5] R. B. Reed, T. Zaikova, A. Barber, M. Simonich, R. Lankone, M. Marco, K. Hristovski, P. Herckes, L. Passantino, D. H. Fairbrother, R. Tanguay, J. F. Ranville, J. E. Hutchison, and P. K. Westerhoff, *Potential Environmental Impacts and Antimicrobial Efficacy of Silver- and Nanosilver-Containing Textiles*, Environmental Science and Technology **50**, 4018 (2016).

[6] C. Wadell, S. Syrenova, and C. Langhammer, *Plasmonic Hydrogen Sensing with Nanostructured Metal Hydrides*, ACS Nano **8**, 11925 (2014).

[7] C. Xiang, Z. She, Y. Zou, J. Cheng, H. Chu, S. Qiu, H. Zhang, L. Sun, and F. Xu, *A room-temperature hydrogen sensor based on Pd nanoparticles doped TiO_2 nanotubes*, Ceramics International **40**, 16343 (2014).

[8] K. S. Novoselov, A. K. Geim, S. V. Morozov, D. Jiang, Y. Zhang, S. V. Dubonos, I. V. Grigorieva, and A. A. Firsov, *Electric Field Effect in Atomically Thin Carbon Films*, Science **306**, 666 (2004).

[9] S. Iijima and T. Ichihashi, *Single-shell carbon nanotubes of 1-nm diameter*, Nature **363**, 603 (1993).

[10] D. Tan and Q. Zhang, *Future Computer, Communication, Control and Automation*, *Advances in Intelligent and Soft Computing* (Springer, Berlin, Heidelberg, 2012), pp. 137–146.

[11] M. Semmler, J. Seitz, F. Erbe, P. Mayer, J. Heyder, G. Oberdörster, and W. G. Kreyling, *Long-Term Clearance Kinetics of Inhaled Ultrafine Insoluble Iridium Particles from the Rat Lung, Including Transient Translocation into Secondary Organs*, Inhalation Toxicology **16**, 453 (2004).

[12] J. F. Hillyer and R. M. Albrecht, *Gastrointestinal persorption and tissue distribution of differently sized colloidal gold nanoparticles*, Journal of Pharmaceutical Sciences **90**, 1927 (2001).

[13] M. Longmire, P. L. Choyke, and H. Kobayashi, *Clearance Properties of Nano-sized Particles and Molecules as Imaging Agents: Considerations and Caveats*, Nanomedicine (Lond) **3**, 703 (2008).

[14] K.-T. Rim, S.-W. Song, and H.-Y. Kim, *Oxidative DNA Damage from Nanoparticle Exposure and Its Application to Workers' Health: A Literature Review*, Saf Health Work **4**, 177 (2013).

[15] M. Faraday, *The Bakerian Lecture: Experimental Relations of Gold (and Other Metals) to Light*, Philosophical Transactions of the Royal Society of London A **147**, 145 (1857).

[16] M. C. Lea, *On allotropic forms of silver*, American Journal of Science **Series 3 Vol. 38**, 47 (1889).

[17] B. Jirgersons and M. E. Straumanis, *A Short Textbook of Colloid Chemistry (Second Revised Edition)* (Pergamon Press, Oxford, 1962), pp. 293–322.

[18] A. Einstein, *On the Movement of Small Particles Suspended in Stationary Liquids Required by the Molecular-Kinetic Theory of Heat*, Annalen der Physik **17**, 549 (1905).

[19] M. Smoluchowski, *Zur kinetischen Theorie der Brown'schen Molekularbewegung und der Suspensionen*, Annalen der Physik **21**, 756 (1906).

[20] G. Mie, *Beiträge zur Optik trüber Medien, speziell kolloidaler Metallösungen*, Annalen der Physik **330**, 377 (1908).

[21] R. Gans, *Über die Form ultramikroskopischer Goldteilchen*, Annales de Physique **342**, 881 (1912).

[22] N. Kumar and S. Kumbhat, *Essentials in Nanoscience and Nanotechnology* (John Wiley & Sons, New Jersey, 2016).

[23] Y. Huttel, *Gas-Phase Synthesis of Nanoparticles* (John Wiley & Sons, New Jersey, 2017).

[24] B. L. Cushing, V. L. Kolesnichenko, and C. J. O'Connor, *Recent Advances in the Liquid-Phase Syntheses of Inorganic Nanoparticles*, Chemical Reviews **104**, 3893 (2004).

[25] J. Turkevich, P. Cooper Stevenson, and J. Hillier, *A study of the nucleation and growth processes in the synthesis of colloidal gold*, Discussions of the Faraday Society **11**, 55 (1951).

[26] N. R. Jana, L. Gearheart, and C. J. Murphy, *Evidence for Seed-Mediated Nucleation in the Chemical Reduction of Gold Salts to Gold Nanoparticles*, Chemistry of Materials **13**, 2313 (2001).

[27] N. R. Jana, L. Gearheart, and C. J. Murphy, *Seeding Growth for Size Control of 5-40 nm Diameter Gold Nanoparticles*, Langmuir **17**, 6782 (2001).

[28] J. Zeng, C. Zhu, J. Tao, M. Jin, H. Zhang, Z.-Y. Li, Y. Zhu, and Y. Xia, *Controlling the Nucleation and Growth of Silver on Palladium Nanocubes by Manipulating the Reaction Kinetics*, Angewandte Chemie International Edition **51**, 2354 (2012).

[29] C. M. Liu, L. Guo, H. B. Xu, Z. Y. Wu, and J. Weber, *Seed-mediated growth and properties of copper nanoparticles, nanoparticle 1D arrays and nanorods*, Microelectronic Engineering **66**, 107 (2003).

[30] G. W. Sławiński and F. P. Zamborini, *Synthesis and Alignment of Silver Nanorods and Nanowires and the Formation of Pt, Pd, and Core/Shell Structures by Galvanic Exchange Directly on Surfaces*, Langmuir **23**, 10357 (2007).

[31] D. Seo, C. I. Yoo, J. Jung, and H. Song, *Ag-Au-Ag Heterometallic Nanorods Formed through Directed Anisotropic Growth*, Journal of the American Chemical Society **130**, 2940 (2008).

[32] C. Gao, J. Goebl, and Y. Yin, *Seeded growth route to noble metal nanostructures*, Journal of Materials Chemistry C **1**, 3898 (2013).

[33] A. S. Barnard and L. A. Curtiss, *Modeling the preferred shape, orientation and aspect ratio of gold nanorods*, Journal of Materials Chemistry **17**, 3315 (2007).

[34] B. Nikoobakht and M. A. El-Sayed, *Preparation and Growth Mechanism of Gold Nanorods (NRs) Using Seed-Mediated Growth Method*, Chemistry of Materials **15**, 1957 (2003).

[35] S. Javadian, V. Ruhi, A. Heydari, A. Asadzadeh Shahir, A. Yousefi, and J. Akbari, *Self-Assembled CTAB Nanostructures in Aqueous/Ionic Liquid Systems: Effects of Hydrogen Bonding*, Industrial & Engineering Chemistry Research **52**, 4517 (2013).

[36] C. J. Johnson, E. Dujardin, S. A. Davis, C. J. Murphy, and S. Mann, *Growth and form of gold nanorods prepared by seed-mediated, surfactant-directed synthesis*, Journal of Materials Chemistry **12**, 1765 (2002).

[37] S. E. Lohse and C. J. Murphy, *The Quest for Shape Control: A History of Gold Nanorod Synthesis*, Chemistry of Materials **25**, 1250 (2013).

[38] E. Carbó-Argibay, B. Rodríguez-González, S. Gómez-Graña, A. Guerrero-Martínez, I. Pastoriza-Santos, J. Pérez-Juste, and L. M. Liz-Marzán, *The Crystalline Structure of Gold Nanorods Revisited: Evidence for Higher-Index Lateral Facets*, Angewandte Chemie International Edition **49**, 9397 (2010).

[39] B. Goris, S. Bals, W. Van den Broek, E. Carbó-Argibay, S. Gómez-Graña, L. M. Liz-Marzán, and G. Van Tendeloo, *Atomic-scale determination of surface facets in gold nanorods*, Nature Materials **11**, 930 (2012).

[40] X. Ye, C. Zheng, J. Chen, Y. Gao, and C. B. Murray, *Using Binary Surfactant Mixtures To Simultaneously Improve the Dimensional Tunability and Monodispersity in the Seeded Growth of Gold Nanorods*, Nano Letters **13**, 765 (2013).

[41] S. Koeppl, C. Solenthaler, W. Caseri, and R. Spolenak, *Towards a Reproducible Synthesis of High Aspect Ratio Gold Nanorods*, Journal of Nanomaterials **2011**, 1 (2011).

[42] C. F. Bohren and D. R. Huffman, *Absorption and Scattering of Light by Small Particles* (Wiley-VCH, Weinheim, 1998), pp. 130–157.

[43] V. Sharma, K. Park, and M. Srinivasarao, *Colloidal dispersion of gold nanorods: Historical background, optical properties, seed-mediated synthesis, shape separation and self-assembly*, Materials Science and Engineering: R: Reports **65**, 1 (2009).

[44] J. N. Israelachvili, *Intermolecular and Surface Forces* (Academic Press, Cambridge, 2015).

[45] H. C. Hamaker, *The London—van der Waals attraction between spherical particles*, Physica **4**, 1058 (1937).

[46] M. R. Wright, *An Introduction to Aqueous Electrolyte Solutions* (John Wiley & Sons, New Jersey, 2007).

[47] V. I. Kalikmanov, *Nucleation Theory*, *Lecture Notes in Physics* (Springer, Dordrecht, 2013), pp. 17–41.

[48] V. K. LaMer and R. H. Dinegar, *Theory, Production and Mechanism of Formation of Monodispersed Hydrosols*, Journal of the American Chemical Society **72**, 4847 (1950).

[49] W. Ostwald, *Studien über die Bildung und Umwandlung fester Körper*, Zeitschrift für physikalische Chemie **22**, 289 (1897).

[50] X.-G. Wang, W. Weiss, S. K. Shaikhutdinov, M. Ritter, M. Petersen, F. Wagner, R. Schlögl, and M. Scheffler, *The Hematite* $\alpha - Fe_2O_3(0001)$ *Surface: Evidence for Domains of Distinct Chemistry*, Physical Review Letters **81**, 1038 (1998).

[51] K. Reuter and M. Scheffler, *Composition, structure, and stability of* $RuO_2(110)$ *as a function of oxygen pressure*, Physical Review B **65**, 035406 (2001).

[52] C. J. Cramer, *Essentials of Computational Chemistry: Theories and Models* (John Wiley & Sons, New Jersey, 2005).

[53] G. Wulff, *Zur Frage der Geschwindigkeit des Wachstums und der Auflösung der Krystallflächen*, Zeitschrift für Krystallographie und Mineralogie **34**, 449 (1901).

[54] R. F. S. Constable, *Kinetics and Mechanism of Crystallization* (Elsevier Science & Technology Books, New York, 1968).

[55] B. Sadigh and P. Erhart, *Calculation of excess free energies of precipitates via direct thermodynamic integration across phase boundaries*, Physical Review B **86**, 134204 (2012).

[56] J. M. Rahm and P. Erhart, *Beyond Magic Numbers: Atomic Scale Equilibrium Nanoparticle Shapes for Any Size*, Nano Letters **17**, 5775 (2017).

[57] C. J. Murphy, T. K. Sau, A. M. Gole, C. J. Orendorff, J. Gao, L. Gou, S. E. Hunyadi, and T. Li, *Anisotropic Metal Nanoparticles: Synthesis, Assembly, and Optical Applications*, Journal of Physical Chemistry B **109**, 13857 (2005).

[58] K. R. Brown, D. G. Walter, and M. J. Natan, *Seeding of Colloidal Au Nanoparticle Solutions. 2. Improved Control of Particle Size and Shape*, Chemistry of Materials **12**, 306 (2000).

[59] A. Gole and C. J. Murphy, *Seed-Mediated Synthesis of Gold Nanorods: Role of the Size and Nature of the Seed*, Chemistry of Materials **16**, 3633 (2004).

[60] J. Gao, C. M. Bender, and C. J. Murphy, *Dependence of the Gold Nanorod Aspect Ratio on the Nature of the Directing Surfactant in Aqueous Solution*, Langmuir **19**, 9065 (2003).

[61] B. Busbee, S. Obare, and C. Murphy, *An Improved Synthesis of High-Aspect-Ratio Gold Nanorods*, Adv. Mater. **15**, 414 (2003).

[62] T. Jain, A. R. Tehrani-Bagha, H. Shekhar, R. Crawford, E. Johnson, K. Nørgaard, K. Holmberg, P. Erhart, and K. Moth-Poulsen, *Anisotropic growth of gold nanoparticles using cationic gemini surfactants: effects of structure variations in head and tail groups*, Journal of Materials Chemistry C **2**, 994 (2014).

[63] H. Lodish, A. Berk, S. L. Zipursky, P. Matsudaira, D. Baltimore, and J. Darnell, *Molecular Cell Biology*, 4th ed. (W. H. Freeman, San Francisco, 2000).

[64] B. Nikoobakht and M. A. El-Sayed, *Evidence for Bilayer Assembly of Cationic Surfactants on the Surface of Gold Nanorods*, Langmuir **17**, 6368 (2001).

[65] T. K. Sau and C. J. Murphy, *Self-Assembly Patterns Formed upon Solvent Evaporation of Aqueous Cetyltrimethylammonium Bromide-Coated Gold Nanoparticles of Various Shapes*, Langmuir **21**, 2923 (2005).

[66] S. Gómez-Graña, F. Hubert, F. Testard, A. Guerrero-Martínez, I. Grillo, L. M. Liz-Marzán, and O. Spalla, *Surfactant (Bi)Layers on Gold Nanorods*, Langmuir **28**, 1453 (2012).

[67] M. K. Kadirov, A. I. Litvinov, I. R. Nizameev, and L. Y. Zakharova, *Adsorption and Premicellar Aggregation of CTAB Molecules and Fabrication of Nanosized Platinum Lattice on the Glass Surface*, Journal of Physical Chemistry C **118**, 19785 (2014).

[68] S. K. Meena and M. Sulpizi, *Understanding the Microscopic Origin of Gold Nanoparticle Anisotropic Growth from Molecular Dynamics Simulations*, Langmuir **29**, 14954 (2013).

[69] S. K. Meena and M. Sulpizi, *From Gold Nanoseeds to Nanorods: The Microscopic Origin of the Anisotropic Growth*, Angewandte Chemie International Edition **55**, 11960 (2016).

[70] S. K. Meena, S. Celiksoy, P. Schäfer, A. Henkel, C. Sönnichsen, and M. Sulpizi, *The role of halide ions in the anisotropic growth of gold nanoparticles: a microscopic, atomistic perspective*, Physical Chemistry Chemical Physics **18**, 13246 (2016).

[71] J. Löfgren, H. Grönbeck, K. Moth-Poulsen, and P. Erhart, *Understanding the Phase Diagram of Self-Assembled Monolayers of Alkanethiolates on Gold*, The Journal of Physical Chemistry. C, Nanomaterials and Interfaces **120**, 12059 (2016).

[72] R. Tran, Z. Xu, B. Radhakrishnan, D. Winston, W. Sun, K. A. Persson, and S. P. Ong, *Surface energies of elemental crystals*, Scientific Data **3**, sdata201680 (2016).

[73] Liu and P. Guyot-Sionnest, *Mechanism of Silver(I)-Assisted Growth of Gold Nanorods and Bipyramids*, Journal of Physical Chemistry B **109**, 22192 (2005).

[74] L. D. Marks, *Modified Wulff constructions for twinned particles*, Journal of Crystal Growth **61**, 556 (1983).

[75] W. Tong, M. J. Walsh, P. Mulvaney, J. Etheridge, and A. M. Funston, *Control of Symmetry Breaking Size and Aspect Ratio in Gold Nanorods: Underlying Role of Silver Nitrate*, Journal of Physical Chemistry C **121**, 3549 (2017).

[76] X. Chen, J. Schröder, S. Hauschild, S. Rosenfeldt, M. Dulle, and S. Förster, *Simultaneous SAXS/WAXS/UV–Vis Study of the Nucleation and Growth of Nanoparticles: A Test of Classical Nucleation Theory*, Langmuir **31**, 11678 (2015).

[77] H. Koerner, R. I. MacCuspie, K. Park, and R. A. Vaia, *In Situ UV/Vis, SAXS, and TEM Study of Single-Phase Gold Nanoparticle Growth*, Chemistry of Materials **24**, 981 (2012).

[78] N. D. Loh, S. Sen, M. Bosman, S. F. Tan, J. Zhong, C. A. Nijhuis, P. Král, P. Matsudaira, and U. Mirsaidov, *Multistep nucleation of nanocrystals in aqueous solution*, Nat Chem **9**, 77 (2017).

[79] J. Polte, T. T. Ahner, F. Delissen, S. Sokolov, F. Emmerling, A. F. Thünemann, and R. Kraehnert, *Mechanism of Gold Nanoparticle Formation in the Classical Citrate Synthesis Method Derived from Coupled In Situ XANES and SAXS Evaluation*, Journal of the American Chemical Society **132**, 1296 (2010).

[80] J. Polte, R. Erler, A. F. Thünemann, S. Sokolov, T. T. Ahner, K. Rademann, F. Emmerling, and R. Kraehnert, *Nucleation and Growth of Gold Nanoparticles Studied via in situ Small Angle X-ray Scattering at Millisecond Time Resolution*, ACS Nano **4**, 1076 (2010).

[81] T. X. Li, Y. L. Ji, S. W. Yu, and G. H. Wang, *Melting properties of noble metal clusters*, Solid State Communications **116**, 547 (2000).

[82] B. S. d. Bas, M. J. Ford, and M. B. Cortie, *Melting in small gold clusters: a density functional molecular dynamics study*, Journal of Physics: Condensed Matter **18**, 55 (2006).

[83] M. Wuithschick, B. Paul, R. Bienert, A. Sarfraz, U. Vainio, M. Sztucki, R. Kraehnert, P. Strasser, K. Rademann, F. Emmerling, and J. Polte, *Size-Controlled Synthesis of Colloidal Silver Nanoparticles Based on Mechanistic Understanding*, Chemistry of Materials **25**, 4679 (2013).

[84] M. Born and R. Oppenheimer, *Zur Quantentheorie der Moleküle*, Annales de Physique **389**, 457 (1927).

[85] P. Hohenberg and W. Kohn, *Inhomogeneous Electron Gas*, Physical Review **136**, B864 (1964).

[86] E. Engel and R. M. Dreizler, *Density Functional Theory*, *Theoretical and Mathematical Physics* (Springer, Berlin, Heidelberg, 2011).

[87] R. M. Martin, *Electronic Structure: Basic Theory and Practical Methods*, 1 ed. (Cambridge University Press, Cambridge, 2004).

[88] W. Kohn and L. J. Sham, *Self-Consistent Equations Including Exchange and Correlation Effects*, Physical Review **140**, A1133 (1965).

[89] J. P. Perdew, K. Burke, and M. Ernzerhof, *Generalized Gradient Approximation Made Simple*, Physical Review Letters **77**, 3865 (1996).

[90] S. Grimme, *Accurate description of van der Waals complexes by density functional theory including empirical corrections*, Journal of Computational Chemistry **25**, 1463 (2004).

[91] J. Klimeš and A. Michaelides, *Perspective: Advances and challenges in treating van der Waals dispersion forces in density functional theory*, The Journal of Chemical Physics **137**, 120901 (2012).

[92] S. Grimme, *Semiempirical GGA-type density functional constructed with a long-range dispersion correction*, Journal of Computational Chemistry **27**, 1787 (2006).

[93] S. Grimme, J. Antony, S. Ehrlich, and H. Krieg, *A consistent and accurate ab initio parametrization of density functional dispersion correction (DFT-D) for the 94 elements H-Pu*, The Journal of Chemical Physics **132**, 154104 (2010).

[94] A. D. Becke and E. R. Johnson, *A density-functional model of the dispersion interaction*, The Journal of Chemical Physics **123**, 154101 (2005).

[95] A. Tkatchenko and M. Scheffler, *Accurate Molecular Van Der Waals Interactions from Ground-State Electron Density and Free-Atom Reference Data*, Physical Review Letters **102**, 073005 (2009).

[96] Y. Zhao and D. G. Truhlar, *Density Functionals for Noncovalent Interaction Energies of Biological Importance*, Journal of Chemical Theory and Computation **3**, 289 (2007).

[97] K. Berland, Doctoral thesis, Chalmers University of Technology, 2012.

[98] K. Berland, V. R. Cooper, K. Lee, E. Schröder, T. Thonhauser, P. Hyldgaard, and B. I. Lundqvist, *van der Waals forces in density functional theory: a review of the vdW-DF method*, Reports on Progress in Physics **78**, 066501 (2015).

[99] G. Román-Pérez and J. M. Soler, *Efficient Implementation of a van der Waals Density Functional: Application to Double-Wall Carbon Nanotubes*, Physical Review Letters **103**, 096102 (2009).

[100] M. Dion, H. Rydberg, E. Schröder, D. C. Langreth, and B. I. Lundqvist, *Van der Waals Density Functional for General Geometries*, Physical Review Letters **92**, 246401 (2004).

[101] Kyuho Lee, Éamonn D. Murray, Lingzhu Kong, Bengt I. Lundqvist, and David C. Langreth, *Higher-accuracy van der Waals density functional*, Physical Review B **82**, (2010).

[102] Y. Zhang and W. Yang, *Comment on "Generalized Gradient Approximation Made Simple"*, Physical Review Letters **80**, 890 (1998).

[103] É. D. Murray, K. Lee, and D. C. Langreth, *Investigation of Exchange Energy Density Functional Accuracy for Interacting Molecules*, Journal of Chemical Theory and Computation **5**, 2754 (2009).

[104] K. Berland and P. Hyldgaard, *Exchange functional that tests the robustness of the plasmon description of the van der Waals density functional*, Physical Review B **89**, 035412 (2014).

[105] L. Gharaee, P. Erhart, and P. Hyldgaard, Per, *Finite-temperature properties of nonmagnetic transition metals: Comparison of the performance of constraint-based semilocal and nonlocal functionals*, Physical Review B **95**, (2017).

[106] N. W. Ashcroft and N. D. Mermin, *Solid State Physics* (Holt, Rinehart and Winston, Geneva, 1976).

[107] P. E. Blöchl, *Projector augmented-wave method*, Physical Review B **50**, 17953 (1994).

[108] G. Kresse and D. Joubert, *From ultrasoft pseudopotentials to the projector augmented-wave method*, Physical Review B **59**, 1758 (1999).

[109] A. Kiejna, G. Kresse, J. Rogal, A. De Sarkar, K. Reuter, and M. Scheffler, *Comparison of the full-potential and frozen-core approximation approaches to density-functional calculations of surfaces*, Physical Review B **73**, 035404 (2006).

[110] H. J. Monkhorst and J. D. Pack, *Special points for Brillouin-zone integrations*, Physical Review B **13**, 5188 (1976).

Paper I

Understanding the Phase Diagram of Self-Assembled Monolayers of Alkanethiolates on Gold

Joakim Löfgren, Henrik Grönbeck, Kasper Moth-Poulsen, and Paul Erhart

The Journal of Physical Chemistry. C, 120, 12059 (2016)

Paper II

libvdwxc: a library for exchange correlation functionals in the vdW-DF family
Ask Hjorth Larsen, Mikael Kuisma, Joakim Löfgren, Yann Pouillon, Paul Erhart, and Per Hyldgaard
Modelling and Simulation in Materials Science and Engineering, 25, 065004 (2017)